

TEMPERATURE PROGRAMMED DESORPTION OF GRAPHENE OXIDE
UNDER ULTRA-HIGH VACUUM

THESIS

Presented to the Graduate Council of
Texas State University-San Marcos
in Partial Fulfillment
of the Requirements

for the Degree

Master of SCIENCE

by

Daniel Alexander Field, B.S.
San Marcos, Texas
December 2008

TEMPERATURE PROGRAMMED DESORPTION OF GRAPHENE OXIDE
UNDER ULTRA-HIGH VACUUM

Committee Members Approved:

Carl Ventrice Jr., Chair

Gregory Spencer

Nikoleta Theodoropoulou

Approved:

J. Michael Willoughby
Dean of the Graduate College

COPYRIGHT

by

Daniel Alexander Field

2008

This thesis is dedicated to Matt Yow. I will always remember the four years of friendship that we were given. We had some very fun times while we were still together. I will never forget the late night talks on the back porch and singing The Piano Man together. You always were there for me whenever I needed you, and for that I thank you. Thank you for your love and friendship.



Mathew "Smitty" Yow
February 26, 1983 - June 4, 2008

ACKNOWLEDGEMENTS

Thank you to my mother and father for the love and support throughout my education, life and while writing this document. I am very happy that you can see me graduate with my master's, and move on to bigger and better things. I would also like to thank Michael, Thomas, and Christie, for being such great siblings through the years. You have all been great friends, and I am very proud to be your baby brother.

I would particularly like to thank Carl for all the time invested in my master's education. Thank you for all the late nights spent working on this document, because I would have never finished without your help. I very much enjoyed working with you in the lab, traveling to Boston, and having you as my professor. I really wish that I would have had more time to finish the graphene oxide project with you. However, I have a feeling that Nick will do a good job.

Thanks to Nick and Robert, for your work on TPD system. Nick, you are quite a programmer; you displayed a large amount of patience while writing the programs, especially trying to find that k-value.

Lastly, I would like to thank all of my friends, wherever they are, for being there for me. In particular I would like to thank Justin and Patrick for the fun we had in San Marcos. I would also like to wish you luck on your research and thesis.

This document was submitted December 9, 2008.

TABLE OF CONTENTS

| | Page |
|--|-------------|
| ACKNOWLEDGEMENTS | v |
| LIST OF FIGURES | viii |
| LIST OF TABLES | x |
| ABSTRACT..... | xi |
| CHAPTER | |
| 1. INTRODUCTION | 1 |
| 2. EXPERIMENTAL..... | 6 |
| 2.1. Ultra-High Vacuum | 6 |
| 2.2. Annealing..... | 9 |
| 2.3. Analysis Techniques | 12 |
| 2.3.1. Low Energy Electron Diffraction | 12 |
| 2.3.2. Atomic Force Microscopy | 16 |
| 2.3.3. X-ray Photoelectron Spectroscopy | 18 |
| 2.4. Temperature Programmed Desorption..... | 20 |
| 2.5. Design and Construction of the Load Lock | 24 |
| 2.6. X-Y-Z Manipulator with Rotary Stage | 28 |
| 2.7. Instrumentation and Computer Programs | 30 |
| 3. RESULTS. | 32 |
| 3.1. Ultra-High Vacuum Reduction of Graphene Oxide | 32 |
| 3.2. Atomic Force Microscopy | 33 |
| 3.3. X-ray Photoelectron Spectroscopy | 34 |
| 3.4. Low Energy Electron Diffraction | 36 |
| 3.5. Temperature Programmed Desorption..... | 40 |
| 3.5.1. ~25 Monolayer Graphene Oxide Crystal | 41 |

| | |
|--|----|
| 3.5.2. ~8 Monolayer Graphene Oxide Crystal | 46 |
| 3.5.3 ~1 Monolayer Graphene Oxide Crystal | 48 |
| 3.6. Desorption Kinetics | 48 |
| 3.7. Activation Energies..... | 51 |
| 4. DISCUSSION. | 54 |
| 5. CONCLUSION..... | 57 |
| APPENDIX..... | 59 |
| REFERENCES | 61 |

LIST OF FIGURES

| Figure | Page |
|---|------|
| 1. Various Models of Graphene Oxide (from ref. [15]). | 3 |
| 2. Schematic of E-beam Heating Filament | 10 |
| 3. Real-space Lattice of Graphite | 13 |
| 4. Reciprocal Lattice of Graphite | 14 |
| 5. Schematic of LEED | 15 |
| 6. Schematic of AFM | 17 |
| 7. Schematic of XPS | 19 |
| 8. Vacuum Chamber and Load Lock | 25 |
| 9. Schematic of Sample Holder | 26 |
| 10. Schematic of Transfer Arm Tip | 27 |
| 11. Schematic of Sample Holder Stage | 29 |
| 12. AFM of Graphene Oxide | 34 |
| 13. O1s and C1s XPS Peaks of Graphene Oxide | 35 |
| 14. LEED Patterns of HOPG. | 37 |
| 15. LEED Patterns of Graphene Oxide | 39 |
| 16. Heating Rate | 40 |
| 17. TPD of ~24ML Graphene Oxide | 42 |
| 18. Corrected TPD for Masses 15, 16, and 17 | 44 |

| | |
|--|----|
| 19. TPD of ~25 Graphene Oxide at Slower Heating Rates | 45 |
| 20. TPD of ~8ML Graphen Oxide | 46 |
| 21. TPD of ~8ML Graphene Oxide at Slower Heating Rates. | 48 |
| 22. TPD of ~1ML Graphene Oxide | 49 |
| 23. TPD Peaks of CO_2 | 50 |
| 24. Activation Energies of Graphene Oxide | 53 |

LIST OF TABLES

| Table | Page |
|---|-------------|
| 1. O1s/C1s Ratios..... | 36 |
| 2. CO ₂ From a ~25ML Film..... | 52 |
| 3. CO ₂ From a ~8ML Film..... | 52 |

ABSTRACT

TEMPERATURE PROGRAMMED DESORPTION OF GRAPHENE OXIDE UNDER ULTRA-HIGH VACUUM

by

Daniel Alexander Field, B.S.

Texas State University-San Marcos

December 2008

SUPERVISING PROFESSOR: CARL VENTRICE JR.

Graphene oxide is an electrical insulator that shows potential for use in nanoscale electronic devices. An understanding of the thermal stability of graphene oxide sheets is important since the electrical, chemical, and mechanical properties of graphene oxide will change as it is reduced at elevated temperatures. In this study, graphene oxide films were grown by deposition of an aqueous solution of graphene oxide onto oxygen plasma cleaned silicon nitride on silicon substrates. The thermal stability of these films was studied by temperature programmed desorption under ultra-high vacuum conditions. The primary decomposition components of the films are H_2O , CO_2 , and CO .

CHAPTER 1

INTRODUCTION

Graphene has been attracting attention in recent years due to its potential for use in nanoscale devices. Graphene is a monolayer thick single sheet of graphite, making it a true two dimensional system. The graphene sheet is the two-dimensional building block of carbon structures of all dimensions, such as three-dimensional graphite, the one-dimensional carbon nanotube, and the zero-dimensional buckyball [1].

Due to the true two-dimensional nature of graphene, its energy band dispersion is predicted to be linear, resulting in a very small effective mass and a very high mobility for electrons and holes at the zero-energy limit (Dirac point) [2,3]. Graphene is superior over other two-dimensional systems because charge carriers can be tuned continuously between electrons and holes in concentrations, n , as high as 10^{13} cm^{-2} and their mobilities, μ , can exceed $15,000 \frac{\text{cm}^2}{\text{V}\cdot\text{s}}$ in ambient conditions [4-7]. However, the mobilities depend on temperature, which means that μ at 300 K is limited by impurity scattering, and therefore can be improved significantly, perhaps, as high as $\sim 100,000 \frac{\text{cm}^2}{\text{V}\cdot\text{s}}$. Other materials exist (InSb at $\sim 77,000 \frac{\text{cm}^2}{\text{V}\cdot\text{s}}$) that have high mobilities at room temperature. However, what makes graphene special is that μ remains high even at high n in both electrically and chemically doped devices, which translates into ballistic transport [1].

The early attempts at isolating graphene concentrated on mechanical or chemical exfoliated graphene, which is labor intensive and provide inconsistent results. There have also been a small number of attempts to grow graphene, using the same approach generally used for the growth of carbon nanotubes. So far, the attempts at growing graphene have resulted in producing graphite films thicker than ≈ 100 layers [8]. On the other hand, single- and few-layer graphene have been grown epitaxially by chemical vapor deposition of hydrocarbons on metal substrates [9,10] and by thermal decomposition of SiC [2,11,12]. Epitaxial graphene is promising for producing linear disperse graphite [2,11], but is extremely costly because it involves the use of single crystal substrates such as SiC (current cost of $\sim \$5k$ per 2" wafer). Therefore, a reliable and cost efficient procedure to produce graphene must be developed before devices made from graphene become practical.

Thin films of graphene oxide and reduced graphene oxide platelets have also recently attracted attention due to their mechanical and optical properties, and its possible use as a dielectric in nanoscale devices [13]. In addition, graphene oxide also shows promise for use as a precursor for the growth of large-scale graphene films by vacuum or chemical reduction.

The extensive chemical oxidation of graphite results in the formation of graphite oxide, which can be exfoliated as graphene oxide layers in an aqueous suspension. The graphene oxide can then be deposited on any desired substrate. This 'graphene oxide paper' [13] is not electrically conductive by electron or hole transport. However, it is possible to make the as-formed graphene oxide film electrically conductive using a chemical or vacuum reduction treatments [14].

Graphene oxide is used in this research as an alternate approach to producing graphene sheets via the thermal reduction of films of graphene oxide platelets in vacuum. The objective of this study was to evaluate any chemical changes and possible graphitization of films composed of graphene oxide sheets due to heat treatment within ultra high vacuum.

Graphene oxide, which has not been studied in great detail, is an interesting material on its own. By tuning the chemistry of the platelets either prior to or after formation of the thin film of overlapped platelets, the film's electrical conductivity, optical properties, or chemical character can in principle also be tuned [14]. The chemical composition and geometric structure of graphene oxide is still unknown. Several different models have been proposed, as shown in Figure 1.



Figure 1: Various models of graphene oxide (from ref. [15]). Notice the hydroxyls and molecular oxygen bound on various models.

Some of these models predict a planar structure, while others favor a buckled structure. Although there is general agreement that the chemical composition of graphene oxide is primarily carbon, oxygen and hydrogen, the assignment and positions of the functional groups of the oxide are still debated. At the surface, epoxide (C-O-C), monoxide (C=O), and/or hydroxyl (C-OH) groups are expected, and carboxylic groups (O=C-OH) are also expected to form on the edges of the platelets and at defects.

Although graphene oxide shows promise for use in several technologically important applications, there are several fundamental questions about its chemical composition, crystal structure, and thermal stability that must be answered before it can be used in practical devices and sensors. Temperature programmed desorption is used in this research so that the chemical and physical properties of graphene oxide can be studied at various stages of thermal reduction, with the ultimate goal of producing large-area, single-layer graphene films.

There have been previous studies of the chemical reduction of exfoliated graphite oxide [16-21]. The results of these studies indicate that it is difficult to regain the electrical properties of graphene with chemical reduction techniques [22]. Most likely, this is because of the introduction of trace amounts of contaminants and possibly from the loss of carbon during the reduction process. However, by performing the reduction under ultra-high vacuum (UHV) conditions, chemical contamination of the film during reduction is eliminated.

The goal of this research project is to measure the decomposition of graphene oxide under UHV conditions. To accomplish this goal, a measurement system for performing TPD studies was designed and constructed. This included a load lock and a sample stage with a thermocouple attached to a thin tungsten wire that acts as a spring clip, permitting direct contact with the sample surface.

TPD analysis requires a linear sample heating rate and the simultaneous measurement of several partial pressures of the desorbing gasses with a quadrupole mass spectrometer. To accomplish this, a computer is used for the control of the temperature ramp and the simultaneous measurement of the partial pressures of the masses being analyzed. A preamp

was built by Robert Kilbourn to amplify and filter the small voltages (typically a few mV) of the thermocouple. A computer program was written by Nicholas Clark to make the temperature ramp linear using a proportional feedback control and to control what masses were recorded.

The TPD measurements show that graphene oxide decomposes at temperatures as low as $\sim 60^{\circ}\text{C}$ and that the main decomposition products are H_2O , CO_2 , and CO . Only very small amounts of O_2 were observed in the TPD spectra, indicating that oxygen only desorbs as H_2O , CO_2 , and CO . An unexpected double peak for the masses of 16 and 17 occurred in the thickest graphene oxide samples. Using the cracking patterns for the masses that were expected to desorb, the double peak was identified as ammonia, which probably comes from the different processing technique used for the thicker samples. Using different sample thicknesses and several heating rates, the decomposition of graphene oxide was revealed to be of second order kinetics. The activation energy was also found to depend on the sample thickness.

X-ray photoelectron spectroscopy (XPS) measurements were also performed on samples annealed in UHV at 500, 700 and 900°C . These results indicate that the graphene oxide was almost completely reduced by 500°C and that graphitization is initiated by $\sim 900^{\circ}\text{C}$ under UHV conditions. However, low energy electron diffraction (LEED) analysis of both the high and low temperature annealed samples showed only a diffuse background, indicating a disordered film. Therefore, the graphene oxide decomposes into a disordered carbon film that only starts to graphitize at very high temperatures. There is also an indication from XPS, agreeing with the TPD spectra, that carbon is being desorbed from graphene oxide.

CHAPTER 2

EXPERIMENTAL

2.1 Ultra High Vacuum

The temperature programmed desorption (TPD), low energy electron diffraction (LEED), and x-ray photoelectron spectroscopy (XPS) measurements for this experiment were all performed in ultra high vacuum (UHV). When a vacuum chamber has a base pressure of $\leq 10^{-9}$ torr, it is considered to be UHV [23]. The chamber used at Texas State University – San Marcos has a base pressure of 6×10^{-11} torr and is designed for performing LEED and TPD measurements. The TPD system is used for measuring the partial pressures of the desorption components of graphene oxide at elevated temperatures. The LEED measurements give the crystal structure of the graphene oxide at various stages of reduction. The XPS measurements, which were taken at the Center for Nano and Molecular Science and Technology at the University of Texas – Austin, in collaboration with Professor Rod Ruoff's research team at the University of Texas, give the chemical composition of the films as a function of anneal temperature.

UHV is very important because it allows ample time for an experiment to be performed without resulting in contamination from the residual gases in the chamber. It can be shown from kinetic gas theory that the number of particles striking, \dot{n}_s , or the gas impingement flux, ϕ , on a surface of 1 cm^2 in 1 second is

$$\phi = \dot{n}_s = \frac{1}{4} N_g \bar{v}, \text{ [Eqn: 1]}$$

where N_g is the number of gas molecules per cm^3 , and \bar{v} is the molecules mean thermal velocity. From this follows the equation

$$\phi = \dot{n}_s = N_g \sqrt{\frac{RT}{2\pi M}} \approx (3.5 \times 10^{22}) \frac{p}{\sqrt{MT}} [\text{cm}^{-2} \text{s}^{-1}], \text{ [Eqn: 2]}$$

where M is the molecular weight, p is the gas pressure, and T is the absolute temperature [24,25]. A simple derivation can be made by assuming a monolayer coverage of $3 \times 10^{14} \frac{\text{particles}}{\text{cm}^2}$, an average molecular weight of 28 and an absolute temperature of 300K, which yields

$$\phi = \dot{n}_s \approx 10^6 \cdot p \left[\frac{\text{monolayers}}{\text{s}} \right]. \text{ [Eqn: 3]}$$

This shows that at a pressure of 10^{-6} torr a monolayer of contaminants will impinge on the surface every second [24].

The coverage time, t_c , depends on the sticking coefficient, s , which is the probability that an impinging molecule is absorbed. Therefore, t_c is given by the function

$$t_c = \frac{1}{\dot{n}_s} \approx \frac{10^{-6}}{s \cdot p}. \text{ [Eqn: 4]}$$

From this equation it can be seen that the vacuum needed to give a measurement time of 1 hour on a surface with $s \approx 1$ without contamination is in the 10^{-10} range. Therefore, it is essential to have UHV to perform surface science experiments.

In order to achieve UHV several different types of pumps are required. The UHV chamber at Texas State uses a rotary vane pump, turbo molecular pump, an ion pump, and a titanium sublimation pump.

The rotary vane pump, which is used to rough pump the chamber and also acts as the backing pump for the turbo molecular pump, is able to achieve $\sim 10^{-3}$ torr within ~ 5 minutes. Rotary vane pumps, although necessary, can contaminate the UHV chamber with backstreaming oil vapor. Nevertheless, a simple zeolite trap is used to prevent this from occurring. The turbo pump, which is popular due to its cleanliness, efficiency, low vibration, and low noise, is able to reach high vacuum within ~ 10 minutes. Once a pressure of $\sim 10^{-6}$ torr is achieved, the ion pump can be used. With these pumps and the ion pump, the chamber can reach $\sim 10^{-9}$ torr. However, to get UHV base pressures suitable for experimentation ($< 10^{-10}$ torr), the chamber must first be baked. The chamber was wrapped in welding blankets and baked at $\sim 150^\circ\text{C}$ for at least 24 hours. Baking the chamber allows the gas and water trapped on the walls to outgas into the chamber allowing them to be removed via the turbo pump and ion pump. After the system is baked, the titanium sublimation pump can be used. This pump is flashed for 1.5 minutes only once a day, which results in a fresh layer of titanium that reacts with the residual gases in the chamber. The titanium sublimation pump's main purpose is to trap hydrogen molecules since it has a much higher pumping speed for hydrogen than the ion pump or turbo pump.

2.2 Annealing

The process of heating a crystal to elevated temperatures is known as annealing. Since the goal of this project is to understand the thermal stability of graphene oxide, the sample holders used in our measurements were capable of heating crystals up to ~1000 °C. The initial annealing measurements were performed with a sample stage that only allowed the mounting of a fixed crystal. The second annealing measurements were performed with a custom-built sample stage that allowed transfer of samples into and out of UHV via a load lock.

The first experiment consisted of mounting graphene oxide samples on the fixed sample holder and measuring the temperature of the crystal with a chromel-alumel thermocouple that was spot welded to a tantalum foil that the sample was attached to. After annealing, the vacuum chamber was vented and the sample was transported to UT Austin to do XPS analysis. Annealing at temperatures up to 500 °C was performed by radiative heating from a tungsten filament mounted behind the tantalum foil. Since this temperature is achieved at the rated maximum current of 4.0A for the filament, e-beam heating was used to achieve annealing temperatures greater than 500°C. For e-beam heating, a high voltage power supply accelerates the electrons from the filament to the sample, as shown in Figure 2.

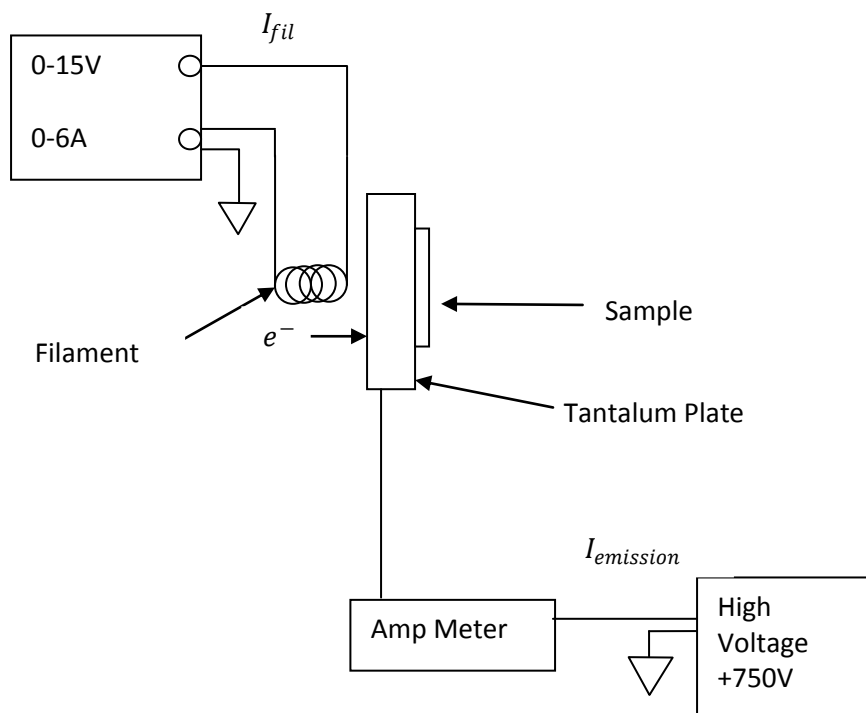


Figure 2: Schematic of the E-beam Heating Filament.

This schematic is for the first three samples that were annealed. The tantalum plate is a solid sheet that does not allow the filament to be directly behind the sample substrate.

Most of kinetic energy of accelerating electrons is then converted to heat on impingement. A sample bias of +750 V causes the accelerated electrons from the filament to be attracted to the sample. Electron beam heating has a very high power density, which allows for very high annealing temperatures. Heating in this manor utilizes the power with greater efficiency than with radiant heating, allowing lower filament currents to be used to reach higher temperatures.

The second experiments involved the design and construction of a sample holder that allowed transfer of samples mounted on a molybdenum plate without breaking UHV

by using a load lock. This TPD experiment used a computer to control the ramping of the sample temperature by radiative heating from a filament. A custom-built thermocouple preamp was designed and constructed to input the signal from the thermocouple to the computer. Since the samples were moved into and out of the UHV chamber, a thermocouple could not be spot welded directly on the molybdenum plate. To measure temperature, a thermocouple was spot welded to a spring-loaded tungsten wire that made thermal contact with the front of the graphene oxide samples. E-beam heating was not used for this part of the experiment since the preamp cannot be used at high voltages.

2.3 Analysis Techniques

To characterize the surface structure and morphology, LEED and AFM were used. To analyze the desorption kinetics and desorption components, TPD and XPS were used. LEED analysis gives a measure of the crystal structure of surfaces. AFM gives a measure of the surface morphology with a resolution of ~1 nm. With TPD, the desorption species are directly measured with a mass spectrometer as a function of sample temperature. XPS provides information about the relative elemental composition of the surface by measuring the areas under the photoemission peaks of the core electrons. The chemical state of each element is determined by measuring the binding energy of each core peak and comparing it to the binding energies of a standard samples.

2.3.1 Low Energy Electron Diffraction

LEED was performed for the analysis of the surface crystallography for each of the annealed graphene oxide samples. LEED is a technique for the determination of the surface structure of crystalline materials by bombardment with a collimated beam of low energy electrons (20-200eV) and observation of the diffracted electrons. Some of the primary electrons are back-scattered from the surface elastically without energy loss. Electrons elastically scattered from a crystal can interfere periodically on the surface because of their de Broglie – wave properties [25].

The electron beam is then represented by a plane wave with a wavelength, λ , in accordance to the de Broglie hypothesis for the wavelength of a matter wave

$$\lambda = \frac{h}{p}, \text{ [Eqn: 5]}$$

where h is Planck's constant and p is the particle's momentum. The corresponding kinetic energy, E , for a nonrelativistic particle is

$$E = \frac{p^2}{2m} = \frac{h^2}{2m\lambda^2} = \frac{\hbar^2 K^2}{2m}, \text{ [Eqn: 6]}$$

where m is the particle mass. Using the mass of an electron, m_e , the electron wavelength, λ_e , is then

$$\lambda_e = \frac{h}{\sqrt{2m_e E}} = \frac{12.3}{\sqrt{E}} \text{ [\AA]}, \text{ [Eqn: 7]}$$

where m_e is the mass of an electron and E is the beam energy in eV [26].

The crystal structure of graphite can be seen in Figure 3 with the real-space lattice vectors of the hexagonal lattice.

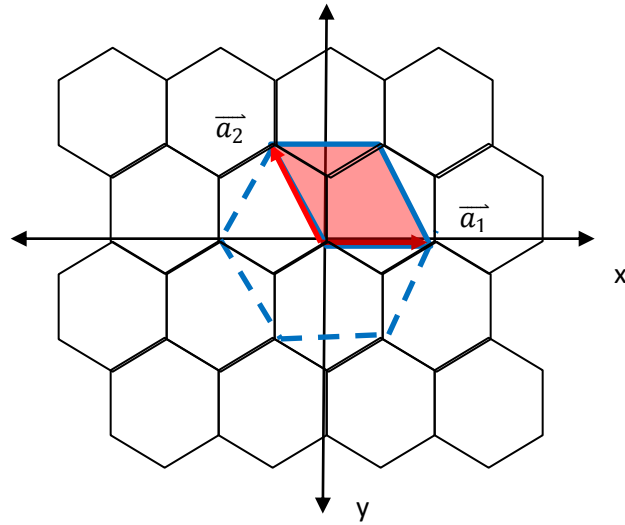


Figure 3: Real-space Lattice of Graphite.

The crystal structure of graphite is shown with the two real-space lattice vectors. The primitive cell of the hexagonal lattice is highlighted.

The real-space lattice has primitive lattice vectors given by

$$\vec{a}_1 = a \hat{i}, \text{ [Eqn: 8]}$$

and

$$\vec{a}_2 = -\frac{a}{2} \hat{i} + \frac{\sqrt{3}}{2} a \hat{j}, \text{ [Eqn: 9]}$$

where a is the lattice constant of graphite (2.462 Å). Therefore, any point of the real space lattice can be connected by a vector given by

$$\vec{R} = m_1 \vec{a}_1 + m_2 \vec{a}_2, \text{ [Eqn:10]}$$

where m_1 and m_2 are integers.

The real-space primitive lattice vectors allow the primitive lattice vectors of the reciprocal lattice to be calculated, giving

$$\vec{b}_1 = 2\pi \left(\frac{2}{a\sqrt{3}} \right) \left(\frac{\sqrt{3}}{2} \hat{i} + \frac{1}{2} \hat{j} \right) \text{ [Eqn: 11]}$$

and

$$\vec{b}_2 = 2\pi \left(\frac{2}{a\sqrt{3}} \right) \hat{j}. \text{ [Eqn: 12]}$$

The points in reciprocal space can be connected by a vector given by

$$\vec{G}_s = n_1 \vec{b}_1 + n_2 \vec{b}_2, \text{ [Eqn: 13]}$$

where n_1 and n_2 are integers.

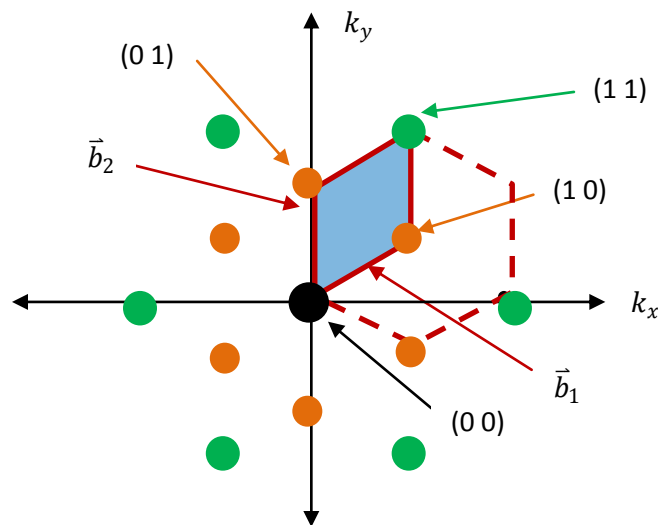


Figure 4: Reciprocal Lattice of Graphite.

The Highlighted area is the primitive cell of the reciprocal lattice. The large dots are the points in reciprocal space that correspond to the diffraction points associated with LEED, with the inner dots being first order and the outer dots being second order.

A constructive interference occurs whenever the change in wave vector of the electron is equal to a reciprocal lattice vector $\Delta\vec{K}_{\parallel} = \vec{G}_s$. This results in the expression

$$\sin\theta = \frac{\pi\hbar\sqrt{2}}{a\sqrt{m_eE}} \sqrt{n_1^2 + \frac{(n_1+2n_2)^2}{3}}, \text{ [Eqn: 14]}$$

for electrons incident normal to the surface, where θ is the angle from the surface normal.

The first order diffraction spots are given by $(1\ 0)$, $(0\ 1)$, $(\bar{1}\ 0)$, $(0\ \bar{1})$, $(1\ \bar{1})$, and $(\bar{1}\ 1)$, and the second order diffraction spots are given by $(1\ 1)$, $(\bar{1}\ 2)$, $(\bar{2}\ 1)$, $(\bar{1}\ \bar{1})$, $(1\ \bar{2})$, and $(2\ \bar{1})$ as shown in Figure 4.

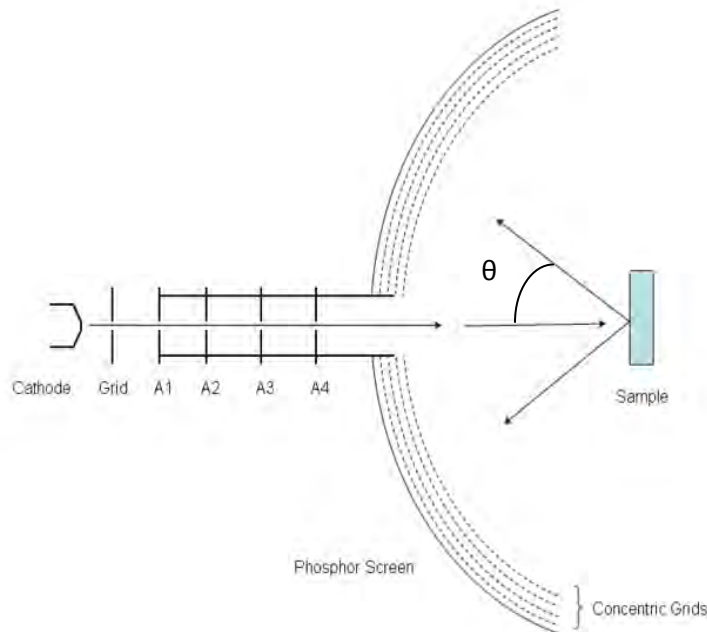


Figure 5: Schematic of LEED.
Where θ is the angle from the surface normal.

LEED can give an indication of the amount of disorder on the sample surface by analyzing the relative intensity of the diffraction spots to the diffuse background, which results from surface disorder. Another factor that must be considered when doing LEED analysis is that insulating samples are subject to sample charging, which is the case for the Si_3N_4 substrate layer. Sample charging can result in a severe distortion of the diffraction pattern.

2.3.2 Atomic Force Microscopy

The AFM is a high-resolution type of scanning probe microscope, with a resolution of less than a nanometer. The image is gathered by scanning the sample surface with a sharp probe at the end of a micro-scale cantilever. Atomic resolution can be obtained by reducing the contact force to $\sim 10^{-9}$ N [27]. This is less than most interatomic forces, limiting tip induced sample deformation and contact area, which allows the imaging of single atoms [27]. Estimating the ionic bond energy $U \leq 10$ eV, a van der Waals bonding energy of $U \leq 10$ meV, and a repulsive force acting of a distance of $\Delta x \approx 0.2\text{\AA}$, the interatomic force

$$F = -\frac{\Delta U}{\Delta x}, \text{ [Eqn: 15]}$$

would be $\leq 10^{-7}$ N for ionic bonds and $\leq 10^{-11}$ N for the van der Waals bond. These forces are in agreement with a typical vibrational frequency

$$\omega = \sqrt{\frac{k_b}{m_a}}, \text{ [Eqn: 16]}$$

where k_b is the interatomic force constant and m_a is the atomic mass. These forces are the requirements for the force constant of the cantilever, $< 0.1 \frac{N}{m}$ [27].

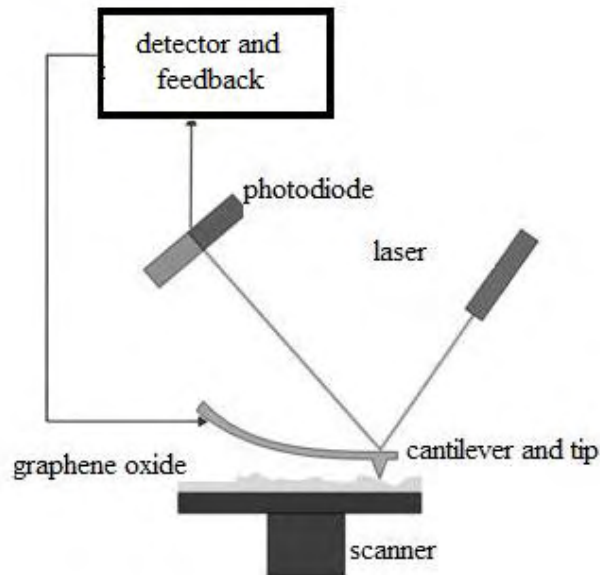


Figure 6: Schematic of AFM.

When the tip is brought into proximity of a sample surface, repulsion forces between the tip and the atomic shells of the sample lead to a deflection of the cantilever providing a true three-dimensional surface profile. Samples viewed by AFM do not require any special treatments that would irreversibly change or damage the sample and can work perfectly well without the need for vacuum.

2.3.3 X-ray Photoelectron Spectroscopy

XPS was also used for the analysis of the composition of the graphene oxide samples before and after annealing. Typical kinetic energies of XPS photoelectrons is 100 eV to 1500 eV, which gives a probe depth of 10-30 Å. With XPS, chemical analysis of the surface is achieved by measuring the binding energies of the core emissions and relative concentrations of the different elements are achieved by measuring the areas under the core emission peaks.

XPS is accomplished by irradiating the sample with monoenergetic soft x-rays. These photons interact with atoms in the surface region, causing electrons to be emitted by the photoelectric effect. The photoelectrons have kinetic energies given by

$$E_k = h\nu - E_b - e\phi_s, \text{ [Eqn: 17]}$$

where $h\nu$ is the energy of the photon, E_b is the binding energy, and $e\phi_s$ is the work function of the spectrometer [28].

By measuring the relative areas under the core electron emission, the concentration of each element can be determined for the sample surface. Chemical shifts occur due to the differences in chemical potential and polarizability of compounds [28]. The chemical state can be obtained by the analysis of these chemical shifts.

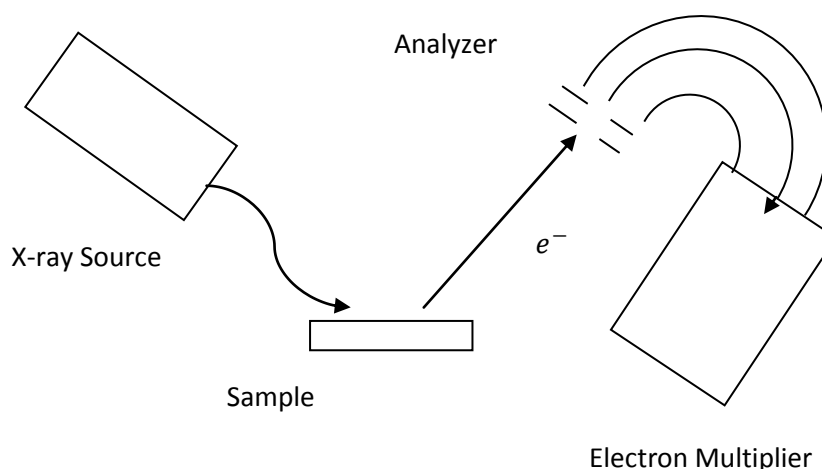


Figure 7: Schematic of XPS.

X-rays are shot onto the sample and the resulting photoelectrons are then focused onto the entrance slit of a concentric hemispherical analyzer. A potential difference is applied between the outer and inner walls of the analyzer, such that an electron with pass energy E_o will be deflected through the analyzer and collected at the detector. Scanning retarding voltage at the entrance of the analyzer while keeping the pass energy constant allows control of the energy of electrons that are allowed to pass through the analyzer and onto the detector, usually a channel electron multiplier.

2.4 Temperature Programed Desorption

Raising the temperature of a sample while obtaining mass spectra via a mass spectrometer of the gases desorbing from its surface is a technique known as temperature programmed desorption. As the temperature rises, a particular molecular species is able to desorb from the surface, causing the pressure to rise. As the temperature rises still further the amount of the species on the surface will eventually reduce causing the pressure to drop again. This results in a peak in the pressure versus temperature plot.

Applying heat to the sample increases the available local energy. The absorbed molecule desorbs when the thermal energy exceeds the activation energy necessary to overcome the adsorbate - substrate interaction [29]. The probability that a molecule will desorb, at any one temperature, to produce an equilibrium vapor pressure, is governed by Boltzmann statistics. This probability that the molecule is in a given microstate is given by the canonical distribution function

$$p(\alpha) = \frac{1}{Z_c} e^{-\beta E} . \text{ [Eqn: 18]}$$

Likewise, if $x(\alpha)$ is the value of some physical property in microstate α , and $E(\alpha)$ is the energy of this state then the *canonical ensemble average* is given by:

$$\langle x \rangle = \frac{1}{Z_c} \sum_{\alpha} x(\alpha) e^{-\beta E(\alpha)} \text{ [29]. [Eqn: 19]}$$

During TPD, the molecules that are being desorbed are monitored by a quadrupole mass spectrometer. This mass spectrometer works by bombarding the gas molecules with electrons to form ions, and these ionized gas molecules are accelerated to a pass energy where they travel through a quadrupole section with an RF field applied,

which acts as a mass selector. The mass spectrometer does not actually measure the molecular mass directly, but rather the mass-to-charge ratio, $\frac{m}{z}$, of the ions formed from the molecules [30]. As a result, the mass spectrum gives a measure of intensity (partial pressures) versus mass-to-charge ratio. The masses recorded can have multiple $\frac{m}{z}$, due to multiple ionization of the molecule and due to the mass spectrometer breaking the molecules into fragments, which is known as “cracking of molecules”. Cracking occurs during the ionization process. Cracking patterns are well documented, providing a unique pattern for each molecule, which allows for mass spectrometry of a sample. Mass spectrometry is a powerful analytical technique that is used to identify unknown compounds, to quantify known compounds, and to elucidate the structure and chemical properties of molecules [30].

TPD also provides quantitative information as it relates to the kinetics of the sample. Kinetic parameters for molecular desorption or reaction on surfaces can be determined by analyzing the desorption spectra within the framework of an assumed model [29]. The kinetics of desorption are often described using approximate forms of a general rate equation, known as the Polanyi-Wigner equation

$$r(\theta) = -\frac{d\theta}{dt} = \nu(\theta)\theta^n e^{-\frac{E_d(\theta)}{RT}}, \text{ [Eqn:20]}$$

where $r(\theta)$ is the rate of desorption, θ represents the surface coverage, t is the time, and ν is the preexponential factor [29]. The kinetics of the material is governed by the reaction order n , where n is typically equal to 0, 1, or 2. Zero order kinetics results from desorption of multilayers of an adsorbate. First order kinetics results from direct

desorption of submonolayer coverages of an adsorbate. If there is recombinative desorption, this is known as second order kinetics. In addition, fractional order kinetics are possible with some samples, giving a reaction order $0 < n < 1$ [29]. Determination of the adsorbate coverage is important when determining the kinetic properties of the sample. With TPD the relative coverages can be obtained by integration of the partial pressure vs. time curve of the desorbed molecule.

The activation energy for desorption, E_d , can be determined by measuring the shift in the temperature of the maximum desorption rate of a molecular species as a function of heating rate. Typically, a linear heating rate is used and it is assumed that there is a uniform substrate temperature and that the desorption energy is independent of the coverage. By substituting a linear temperature ramp function, $T_0 + \beta t$, into the Polanyi-Wigner equation and differentiating with respect to time, t , and then setting the result equal to zero, the following relations

$$\frac{E_d}{RT_p^2} = \frac{\nu}{\beta} e^{-\frac{E_d}{RT_p}} \quad [\text{Eqn: 21}]$$

and

$$\frac{E_d}{RT_p^2} = 2 \frac{\Theta_0}{\beta} \nu e^{-\frac{E_d}{RT_p}} \quad [\text{Eqn: 22}]$$

can be found, where $n = 1$ and $n = 2$, respectively [29]. The temperature T_p is where the plot of rate versus T reaches its maximum. For 1st and 2nd order kinetics, the desorption equation can be written as

$$\ln\left(\frac{T_p^2}{\beta}\right) = \frac{E_d}{RT_p} - \ln\left(\frac{E_d}{vR}\right) \text{ [Eqn: 23]}$$

and

$$\ln\left(\frac{T_p^2}{\beta}\right) = \frac{E_d}{RT_p} - \ln\left(\frac{2vR\theta_0}{E_d}\right). \text{ [Eqn: 24]}$$

Therefore, by plotting $\ln\left(\frac{T_p^2}{\beta}\right)$ as a function of $\frac{1}{T_p}$, the desorption energy can be determined. This method of determining the desorption energy for a particular molecule is known as the Redhead method [30].

The activation energy or desorption energy may otherwise be denoted as the minimum energy necessary for a specific chemical reaction to occur, or in the case of TPD the desorption to occur. For desorption, the activation energy roughly corresponds to the height of the potential barrier, at which the transition state along a reaction coordinate is the point of maximum free energy, where bond-making and bond-breaking are balanced.

2.5 Design and Construction of the Load Lock

Since previous data from Yang et al. [31] shows that desorption from graphene oxide occurs at temperatures below 200°C and temperatures as high as 180°C are reached during the bake out process of the UHV chamber, it was necessary to incorporate a load lock into the UHV system at Texas State. This allows TPD measurements of graphene oxide samples that have not undergone any previous thermal treatment. The addition of a load lock also increased the through put of samples. Without the load lock, only one sample could be measured each week since the chamber needed to be baked out to achieve UHV after insertion of a new sample.

The load lock system consists of a load lock chamber, a magnetic transfer arm, and a frame to support the chamber and transfer arm, as shown in Figure 6. Both the load lock chamber and the frame were machined and welded at Texas State using the machining and welding equipment in the Physics machine shop and the Surface Science laboratory. By custom building these components, there is an opportunity to add other useful features to the system for future studies. The load lock system is pumped by a turbo pump backed by a rotary vane pump.

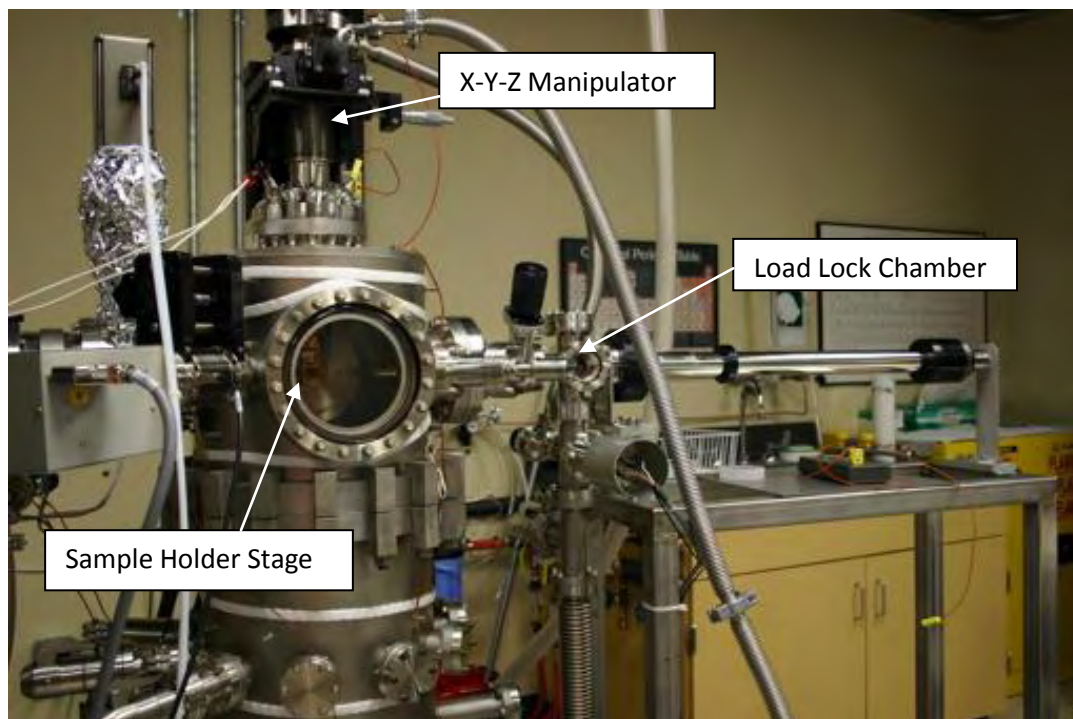


Figure 8: Vacuum Chamber and Load Lock.

The sample holder, which was specifically designed for simplicity, is machined from a of a 0.90" x 1.20" x 0.10" piece of pure molybdenum. A cantilever in the shape of an 'L' was machined into one of the sides, which is what allowed the sample holder to be clasped by the transfer arm. A schematic of the sample holder is shown in Figure 9.

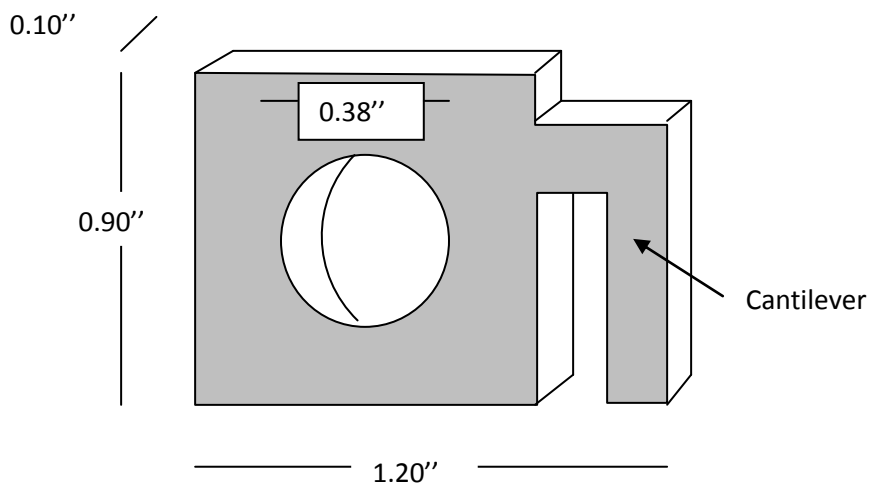


Figure 9: Schematic of Sample Holder. The hole in the center allows the heating filament to be directly behind the sample substrate.

A 0.38" diameter hole was machined into the center of the sample holder, which allowed the heating filament to heat the sample without having to conduct through the molybdenum sample holder. This permits a higher heating range for both radiant and e-beam heating during the TPD process.

The magnetic transfer arm had to be modified to hold the sample holder which was designed for the TPD system. A transfer arm tip was designed from a 1/2" inch solid beryllium copper rod. Beryllium copper, which is the hardest alloy of copper, was used to prevent seizing of the sample holder during transfer to the x,y,z manipulator.

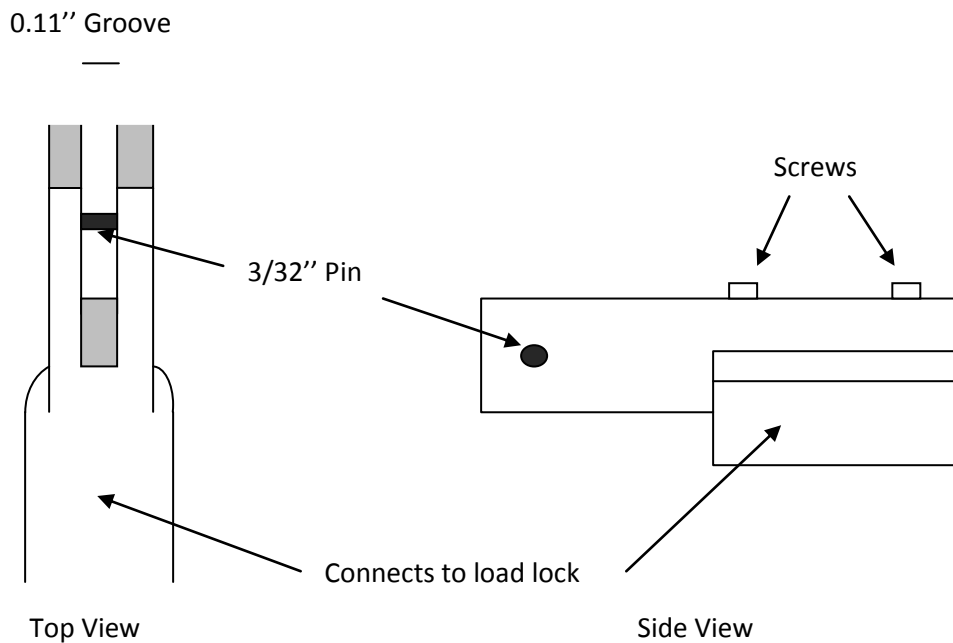


Figure 10: Schematic of Transfer Arm Tip.

The end of the beryllium copper rod that would grasp the sample holder was squared. A groove was cut completely through the center of the squared end to hold the sample holder in place. The groove was cut 0.010'' wider than the 0.10'' width of the sample holder cantilever. This allowed for a firm grip on the sample holder while allowing smooth loading and unloading during sample transfer. A 3/32'' diameter pin was placed perpendicular to the groove of the beryllium copper piece to support for the sample holder's cantilever. The opposing end of the beryllium copper rod was cut into a half cylinder for attachment to the actual stainless steel transfer arm. A schematic of the transfer arm tip is shown in Figure 10.

2.6 X-Y-Z Manipulator with Rotary Stage

The initial annealing experiments for the XPS analysis were done using an existing Varian x,y,z , manipulator. However, the incorporation of a load lock with sample transfer required the redesign of the x,y,z stage. A new x,y,z manipulator with 1” of x and y travel and 2” of z travel was installed with a differentially pumped rotary motion feedthru. In addition, a specially designed sample holder stage was built to allow transfer of the new sample holder. The sample holder stage was made from oxygen-free high conductivity (OFHC) copper, which has a high thermal conductivity and prevents the molybdenum sample holder from seizing during the sample transfer. The high thermal conductivity was not necessary for TPD; however, it plays an essential role in sample cooling for future experiments. The sample holder stage is attached to a stainless steel tub that is welded to a conflat flange that is attached to the rotary motion feedthru. The stainless steel tube, which acts as a dewar, can be filled with liquid nitrogen for low temperature experiments. By blowing compressed air into the dewar during the TPD measurements, the manipulator temperature is kept from overheating while annealing the sample.

The sample holder is held to the sample holder stage by two strips of 0.006” molybdenum foil that were bent to act as springs. These strips also serve as backstops to prevent over shooting during the sample transfer. The strips were strong enough to secure the sample holder firmly to the sample holder stage yet small enough to not create extra friction which would have lead to seizing during transfer.

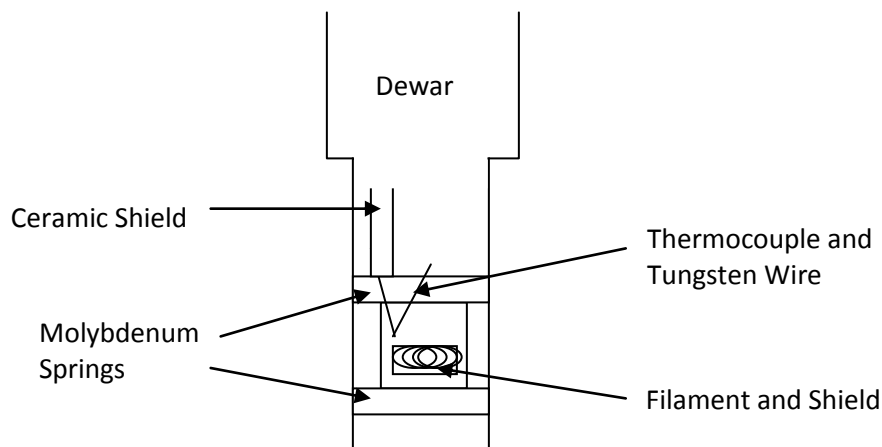


Figure 11: Schematic of Sample Holder Stage.

The sample holder slides in between the molybdenum springs. This allows the thermocouple to touch the sample. The filament is then directly behind the sample substrate.

The sample holder stage in Figure 11 has a 0.5" by 0.5" square hole directly behind the sample, allowing the heating filament to sit directly behind the sample, thus heating the sample without having to conduct through the copper. The heating filament used was removed from a standard 12V, 50 W light bulb. The glass of the bulb was completely removed, and the filament was cut from the electrical contacts. Tantalum rod replaced the tungsten contacts that the bulb used. A macor ceramic piece was machined to firmly hold and electrically isolate the tantalum contacts.

A tantalum shield was spot welded to one of the filament rods and extended around the filament. This prevents direct heating of the copper during electron beam heating. Tantalum is ideal for the shield because it is a good electrical conductor and has a very high melting point. Therefore, it will prevent the copper from conducting the electrons during electron beam heating and can withstand tremendous heat.

Most TPD systems attach the thermocouple to the sample holder stage, near the sample. Since the actual temperature of the graphene oxide is essential for accurate TPD measurements, a unique thermocouple mount that makes direct thermal contact with the front of the sample was designed and built. A 0.010" tungsten wire acts as a spring that slides across the front of the sample as the sample is inserted. A 0.005" chromel-alumel, type K, thermocouple is spot welded to the tungsten spring at the point of contact with the graphene oxide sample. The thermocouple, where it attaches to the sample holder stage, is sheathed in a ceramic tube, to prevent it from shorting to the sample holder stage. The ceramic is an insulator which requires it to be wrapped in a tantalum foil to prevent charging when LEED is being performed.

2.7 Instrumentation and Computer Programs

The TPD system uses a *Hiden Analytical*, HAL 201, quadrupole mass spectrometer, which is mounted on a linear translator with 2" of travel. By mounting the mass spectrometer on a linear translator, it permitted the mass spectrometer to be moved within a few millimeters of the front of the sample. A shield is attached on the end of the mass spectrometer, which allows the desorbing gases from the front of the sample to enter the mass spectrometer, rather than residual gas desorbing within the chamber.

The mass spectrometer and the filament power supply were both programmable allowing for a computer controlled temperature ramp and pressure readings. A *National Instruments* data acquisition board (*NI 6025E*) was installed to permit the computer to control the mass spectrometer and the filament power supply and to measure the

temperature of the sample. In order for the computer to read the small voltages outputted by the thermocouple, a preamp and interface unit was built by Robert Kilbourn. The preamp has a gain of 100 and also incorporates an RC filter with a cutoff frequency of 16 Hz. The conversion from the output of the thermocouple in millivolts to a temperature in °C is calculated by the computer by using an empirical formula [32]. Using *National Instruments LabVIEW 8.0*, a computer program was created, by Nicholas Clark, to increase the temperature linearly, while recording the partial pressures of the desired masses from the mass spectrometer.

The temperature ramp was controlled by adjusting the current through the filament by using a proportional feedback system. The maximum current output was set at 4A to prevent failure of the filament. Due to the particular *NI* device installed in the computer, it was not possible to have partial pressure and temperature correlate within the same program. Therefore, two programs were created linking temperature and pressure, via the computer's inner clock, allowing for their comparison during data analysis.

CHAPTER 3

RESULTS

3.1 Ultra-High Vacuum Reduction of Graphene Oxide

The initial studies of the thermal decomposition of graphene oxide were performed by annealing films in UHV, followed by *in-situ* LEED analysis and *ex-situ* AFM analysis. Each sample was heated to their respective final temperature of 500°C, 700°C, and 900°C, using a manually increased temperature ramp. The temperatures were calculated using thermocouple temperature conversion charts having final voltages of 20.6mV, 29.5mV, and 32.8mV, which correspond to 500°C, 700°C, and 900°C, respectively. The pressure of the chamber at the start of each anneal was $\sim 9.0 \times 10^{-11}$ torr and an initial current of ~ 2.0 A was used for the heating filament. Once the desired temperature was reached the sample was maintained at the final temperature for 15 minutes. The current was then decreased, allowing the sample to cool to room temperature.

After the sample transfer mechanism, new sample holder, and TPD interface and program were completed, a series of TPD measurements were performed on samples with three different thicknesses (~ 1 ML, ~ 8 ML, and ~ 25 ML). The samples were prepared by the University of Texas group by depositing an aqueous solution of graphene oxide onto Si_3N_4 coated Si(100) substrates. The thin films (~ 1 ML and ~ 8 ML) were

exfoliated from graphite oxide by slow stirring in water, whereas the thicker films were exfoliated by ultrasonication, resulting in smaller graphene oxide platelets. In addition, LEED was performed on samples before and after the annealing of some of the samples.

3.2 Atomic Force Microscopy

AFM images of both the pre-annealed graphene oxide film and the film after anneal to 500 °C and 700°C are shown in Figure 12. For the pre-annealed film, the individual nanoscale graphene oxide sheets are observed (Fig 12a). The sheets of graphene oxide are spread randomly on the substrate, producing layers of different thicknesses. For the annealed films, the surface morphology changes from a collection of individual sheets before the anneal to a random arrangement of rounded features on the surface at 700 °C. Therefore, the fully reduced graphene oxide is probably more representative of disordered carbon than ordered graphene. At 500°C, there are several pyramidal structures observed on the surface that disappear at 700°C.

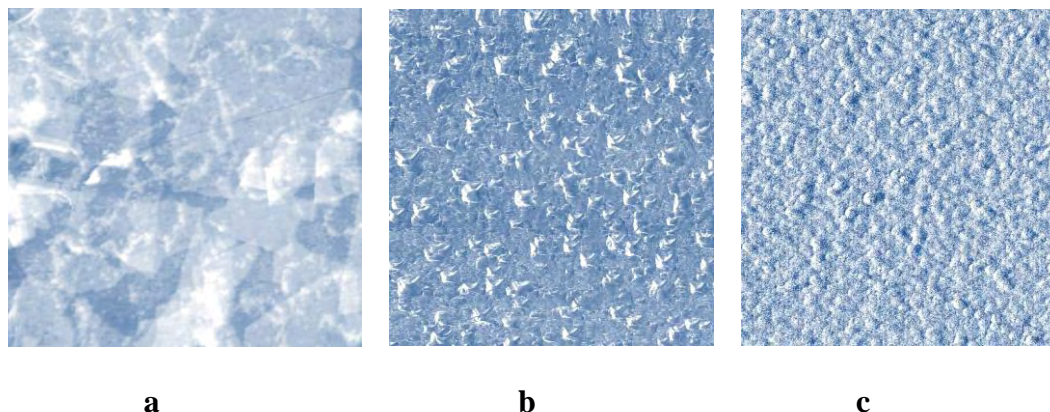


Figure 12: AFM of Graphene Oxide.

AFM images of pre-annealed (a), 500°C annealed, and 700°C annealed graphene oxide.

3.3 X-ray Photoelectron Spectroscopy

After the annealing treatments and LEED were performed, the samples were removed from UHV into atmosphere and transported to the University of Texas for XPS characterization. The XPS measurements were performed with an *Omicron* ESCA Probe. Al $K\alpha$ x-rays were used which have an energy of $h\nu = 1486.6\text{eV}$. The XPS data curve fitting of the C1s and O1s spectra was performed using a Gaussian-Lorentzian peak shape after a Shirley background correction. A binding energy of 284.5-285eV was assigned to the C-C and C-H bonds and chemical shifts of +1.5, +2.5, and +4.0 were assigned to the C-OH, C=O, and O=C-OH functional groups.

The C1s spectrum has double peaks with a main peak at 285.1eV, and another peak at 287.7eV. The 287.7eV peak can be fit to the peaks at 286.4, 287.8 and 288.9 eV which are assigned to C-OH, C-O, and O=C-OH species, respectively. Likewise, the

O1s spectrum also has double peaks. The peak at 530.6eV is assigned to contributions from C=O and O=C–OH groups, and the peak at 533eV to C–OH group.

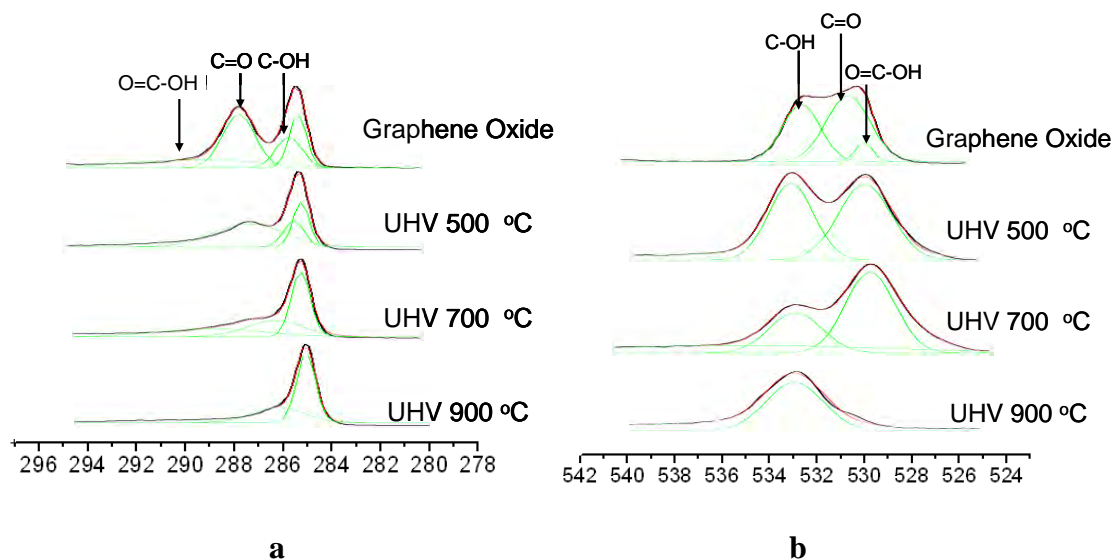


Figure 13: C1s and O1s XPS peaks of Graphene Oxide.

XPS peaks for the C1s (a) and O1s (b) for graphene oxide pre-annealed and annealed to 500, 700, and 900°C.

The C1s peak at 287.7eV decreased in intensity following the 500°C and 700°C treatment, and completely disappeared after the 900°C treatment. The O1s peak at 530.6eV is observed at 529.2eV after both the 500°C and 700°C treatments, indicating a chemical conversion of the C=O and O=C–OH groups to a new chemical species. This peak completely disappears after the 900°C treatment.

The atomic ratio of carbon to oxygen, O1s/C1s, was calculated by taking the area of the C1s peak divided by area of the O1s peak, multiplied by the ratio of the photoionization cross sections from the XPS survey spectrum. The O1s/C1s ratios, seen

in Table 1 decreased as a result to each annealing treatment, indicating a reduction in the graphene oxide film.

Table 1: O1s/C1s ratios obtained by XPS

| As-deposited | 500 °C Anneal | 700 °C Anneal | 900 °C |
|---------------|---------------|----------------|----------------|
| 2.8 ± 0.1 | 8.9 ± 0.2 | 13.2 ± 0.3 | 14.1 ± 0.3 |

It will be evident from the TPD results that most of the hydroxyl and oxide groups are desorbed well before 500°C. However, the samples were exposed to atmosphere for the transport to the XPS measurement system, which probably results in adsorption of water and hydroxyl groups and possibly a partial reoxidation of the reduced carbon layer. The XPS data in Table 1 show that there was a reduction in the oxygen uptake as the final anneal temperature was increased, indicating that they are more inert to ambient air. This is a possible indication that the reduced graphene oxide layer starts to recrystallize into graphene as the final anneal temperature increased.

3.4 Low Energy Electron Diffraction

LEED was performed on the graphene oxide crystals after annealing to 500 °C, 700 °C, and 900 °C and was also performed on the pre-annealed graphene oxide sample that was subsequently annealed to 500 °C. The screen voltage was set at 3kV and the emission current at ~2mA. The beam energy is varied from 50-300eV during the measurements. As a reference for the expected LEED images of graphene, LEED images

from a highly-ordered pyrolytic graphite (HOPG) sample were taken and are shown in Figure 14.

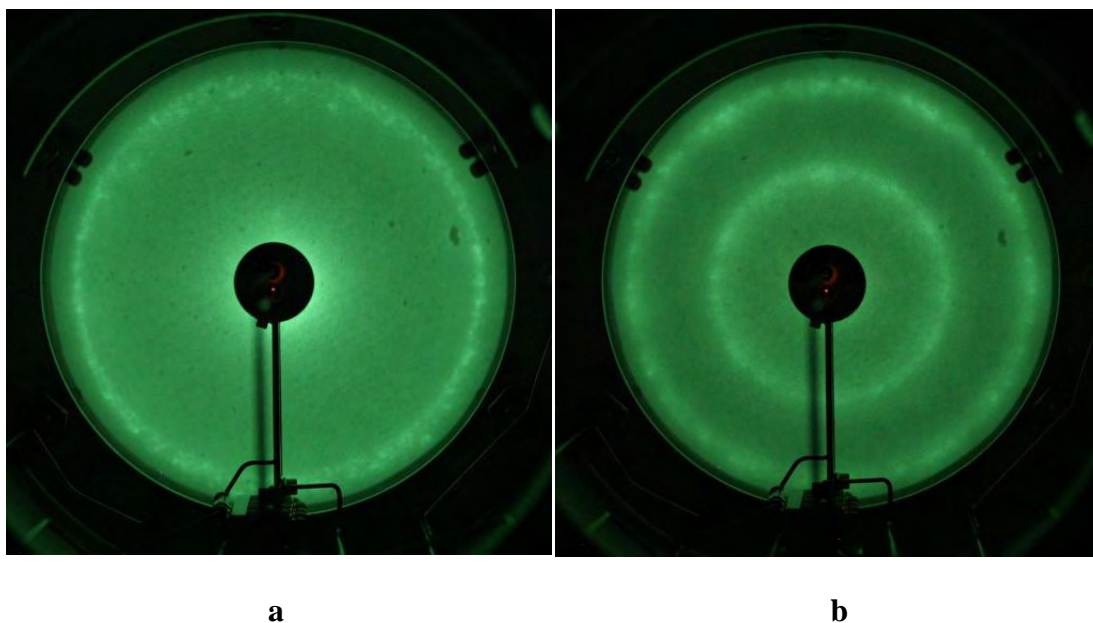


Figure 14: LEED Patterns of HOPG.
LEED patterns of HOPG at 70eV (a) and 194eV (b).

The LEED pattern of the HOPG at 70 eV shows a single ring pattern (Fig 14a), consisting of several diffraction spots that correspond to the multiple domains of the HOPG crystallites. The LEED pattern of the HOPG at 194 eV shows two ring patterns (Fig 14b), which correspond to the 1st and 2nd order diffraction rings. The expected energies at which the 1st order and 2nd order diffraction “rings” should appear on the LEED screen are calculated using Equation 14, which results in values of 44eV and 133eV, respectively for a graphite lattice constant of $a = 2.462\text{\AA}$ and $\theta_{max} = 60^\circ$. The LEED pattern of the pre-annealed graphene oxide film showed no diffraction spots and a

large amount of diffuse background, which indicates that the graphene oxide does not exhibit any long-range order. The LEED performed after the high temperature anneals often resulted in sample charging, indicating that the carbon or graphene layer is not continuous over the whole surface after reduction. In other words, the insulating Si_3N_4 layer is partially exposed after reduction of the graphene oxide.

LEED analysis was also performed before and after TPD measurements on some of the graphene oxide samples. The maximum temperature achieved with TPD is ~ 350 °C because the samples were only heated using radiative heat transfer from the filament instead of e-beam heating, which is used for the higher temperature anneals. As mentioned in the Experimental section, e-beam heating could not be used for the TPD measurements since it requires that the sample be held at high voltage, which would damage the temperature measurement preamp. A LEED image of a graphene oxide film before anneal and after TPD measurement is shown in Figure 15.

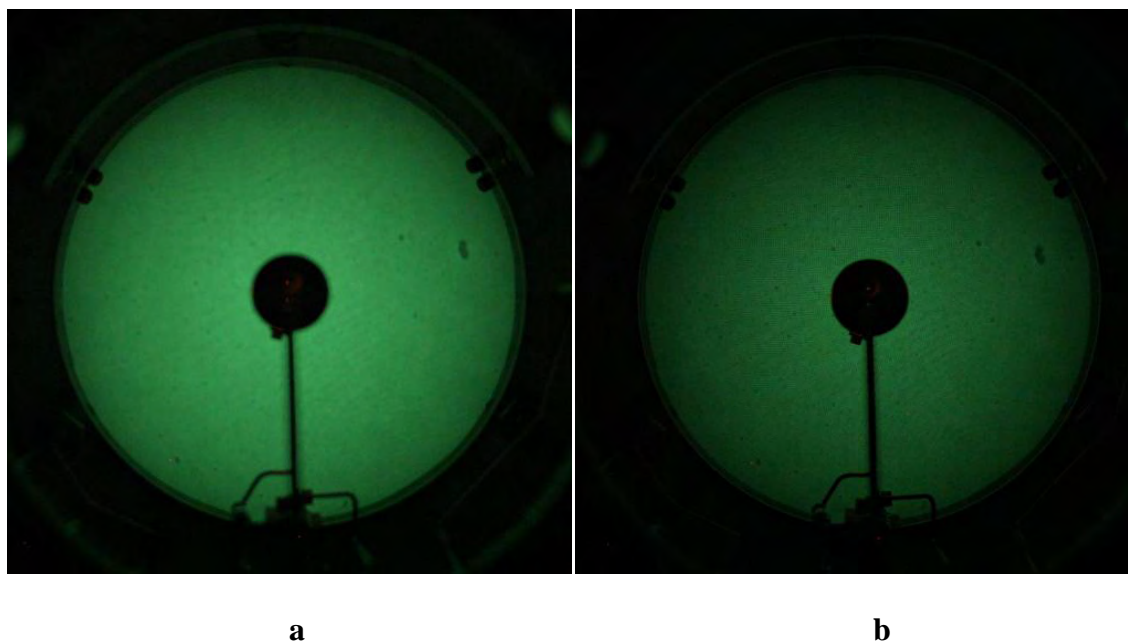


Figure 15: LEED Patterns of Graphene Oxide.

Diffuse backgrounds from LEED on graphene oxide pre-anneal (a) and after 400°C anneal (b).

Neither the LEED pattern of the graphene oxide before nor the one after the TPD measurement shows any diffraction spots. However, the pattern before anneal (Fig 15a) shows a larger amount of diffuse background, which may result from a buckling of the graphene oxide sheets that form the film. Since the temperature reached in TPD measurements was not high enough to cause graphitization, no diffraction rings are observed in Figure 15b.

3.5 Temperature Programmed Desorption

The TPD measurements were performed on graphene oxide films deposited on SiO₂, with three different thicknesses: ~25, ~8, and ~1ML. The film thicknesses were determined by the UT group using ellipsometry. In order to calculate activation energies, the heating rates of the samples were kept constant by using a proportional feedback control. The maximum temperature of the linear region was ~300°C. A temperature versus time graph can be seen in Figure 16.

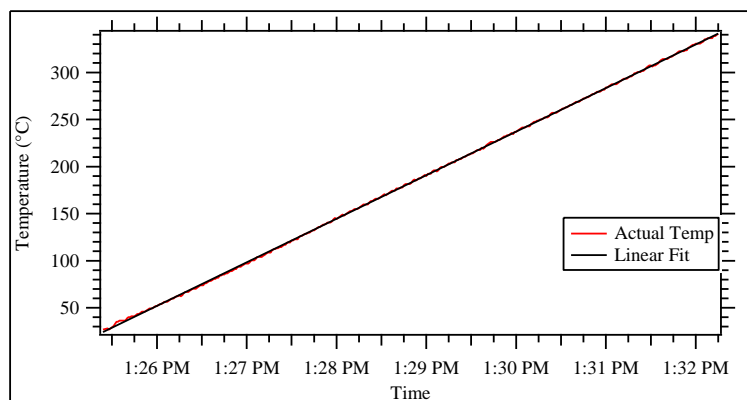


Figure 16: Heating Rate.
Linear temperature ramp of the TPD system.

For the ~25 ML and ~8 ML films, three nominal heating rates were used: 50, 25, and 10 $\frac{^{\circ}\text{C}}{\text{min}}$. Since the partial pressures of the desorbing gases was very low for the ~1 ML film, only data at 25 $\frac{^{\circ}\text{C}}{\text{min}}$ were taken. The partial pressures of masses 12, 15, 16, 17, 18, 28, 32, and 44 were measured by the TPD program. The masses 44, 32, 28, and 18 correspond to the desorption of CO₂, O₂, CO, and H₂O, respectively. Masses 17, 16, 15, and 12 correspond to cracking components of the desorbing gases.

The pressure versus temperature spectra was obtained, using *Igor Pro*, by applying a linear fit to the temperature versus time curve. The obtained line equation was then applied to the pressure versus time curve, allowing the pressure to correlate with temperature.

For all the spectra obtained a small peak of carbon monoxide, mass 28, exists at the start of the spectrum. Due to the consistency of the desorption temperature and the fact that the partial pressure is thickness independent, it was concluded that this peak was due to CO emission from the filament when it turns on and is not a desorption component of the graphene oxide at that temperature.

3.5.1 ~25 Monolayer Graphene Oxide Crystal

A set of TPD spectra for a ~25ML sample heated at $\sim 50 \frac{^{\circ}\text{C}}{\text{min}}$ is shown in Figure 17. For this sample thickness and heating rate, the maximum of the desorption peaks occurs at 103°C. The masses with the highest peaks were 18, 44, and 28, corresponding to water, carbon dioxide, and carbon monoxide molecules.

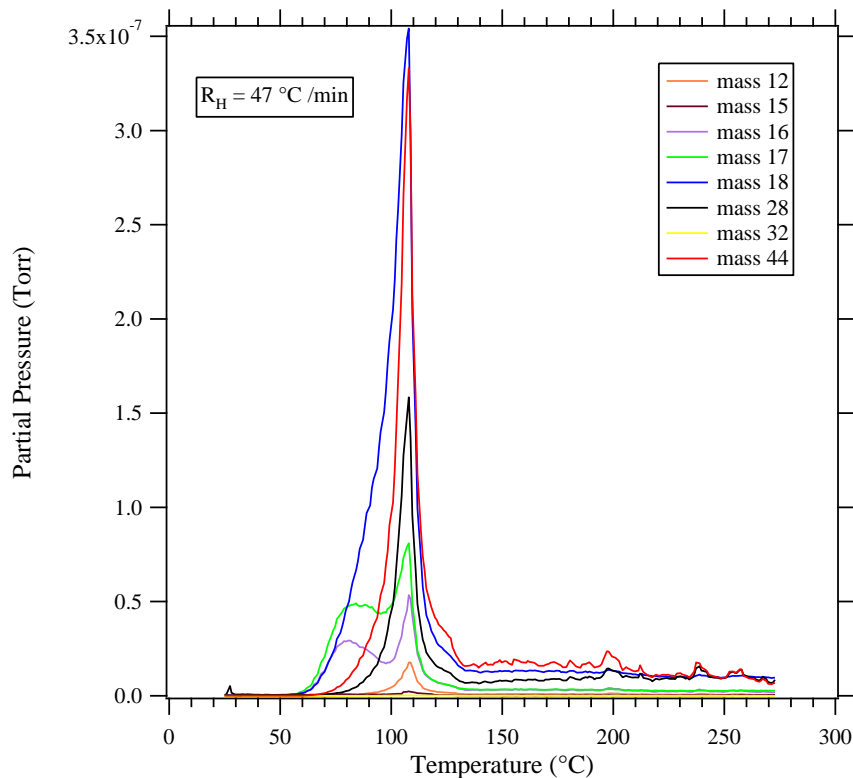


Figure 17: TPD of ~25ML Graphene Oxide.
 TPD spectrum of graphene oxide at a heating rate of
 $\sim 50 \frac{^\circ\text{C}}{\text{min}}$.

The onset of desorption occurs at $\sim 60^\circ\text{C}$ and continues to $\sim 130^\circ\text{C}$, indicating that the graphene oxide decomposes at relatively low temperatures. Virtually no mass 32 (molecular oxygen) was detected over this temperature range. By measuring the areas under the pressure-time curves and correcting for the different RGA sensitivities for water, carbon dioxide and carbon monoxide (0.9, 1.4, 1.05, respectively), the relative amount of carbon dioxide to water and carbon monoxide to water were determined to be 0.53 and 0.32, respectively.

An unexpected double desorption peak occurs for the masses 16 and 17. The first peak occurs at $\sim 80^\circ\text{C}$ and the second occurs at 103°C . The partial pressure of mass 17 is associated with the cracking of water molecules into hydroxyl groups, *OH*. The partial pressure of mass 17 should be 18% of the intensity of the mass 18 partial pressure (see Appendix). Mass 16 is also a cracking fragment of water (atomic oxygen) and has a relative intensity of 2%. It is also a cracking fragment of CO_2 and CO , with relative intensities of 9% and 2%. By subtracting the expected partial pressures of O and OH that result from cracking of CO_2 , CO , and H_2O from the mass 17 and 16 spectra, the resultant partial pressure spectra are obtained as shown in Figure 18. As expected, the peaks at 103°C are almost entirely gone. However, the peaks at $\sim 80^\circ\text{C}$ remain, which indicates that there is either direct desorption of OH and O from the surface or there is desorption of another molecular species from the surface with cracking fragments at masses 17 and 16.

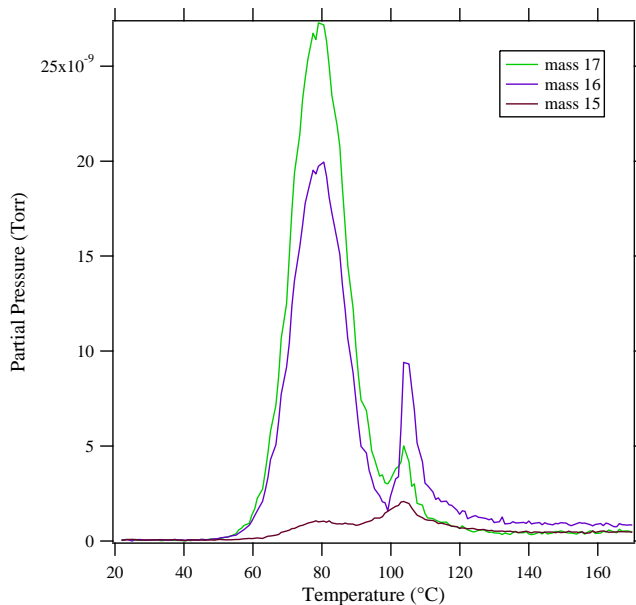


Figure 18: Corrected TPD of Masses 15, 16, and 17.

TPD spectrum of masses 15, 16, and 17 after accounting for cracking corrections seen in the appendix.

Since the mass 16 peak is not accompanied by a peak at mass 32 (molecular oxygen), it is believed that the mass 16 peak is not due to atomic oxygen. The ratio of the mass 16 to mass 17 peak heights is 0.73, which is reasonably close to the expected ratio of 0.8 for ammonia (NH_3). If ammonia were present, there should also be a mass 15 peak with a relative height of 0.08 to the peak height of mass 17. The ratio of mass 15 to mass 17 peak heights is only 0.03. However, relative to the other masses, the base partial pressure for mass 15 is much lower. Therefore, it can be argued that the spectrum for mass 15 is not as precise, and the 5 percent difference fits within the margin of error. The source of the ammonia is not known but was probably introduced during the exfoliation stage of the graphene oxide production by the University of Texas group.

The TPD spectra of samples heated at a rate of ~ 10 and $\sim 25 \frac{\text{°C}}{\text{min}}$ are shown in Figure 17. These spectra are similar to the spectra of the $50 \frac{\text{°C}}{\text{min}}$ sample, including the double peaks of masses 16 and 17.

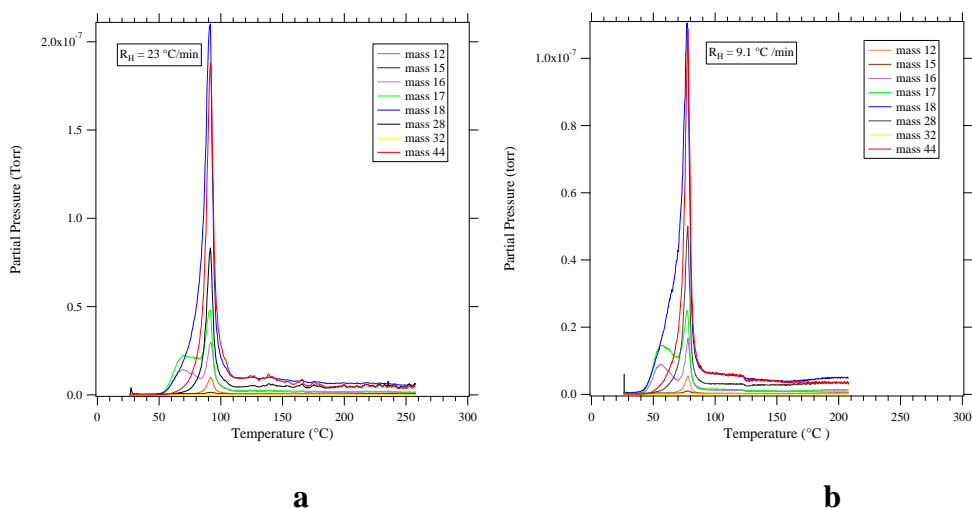


Figure 19: TPD of ~ 25 Graphene Oxide at Slower Heating Rates.

TPD spectrum of ~ 25 ML graphene oxide with heating rates of $\sim 25 \frac{\text{°C}}{\text{min}}$ (a) and $\sim 10 \frac{\text{°C}}{\text{min}}$ (b). Notice the shift in the desorption peaks to a lower temperature.

The primary difference between the spectra of these three samples is the temperature shifts of the main desorption peaks to 91 °C for the heating rate of $\sim 25 \frac{\text{°C}}{\text{min}}$ and 78 °C for the heating rate of $\sim 10 \frac{\text{°C}}{\text{min}}$. The shifts of the desorption maxima to lower temperatures result from the longer heating time, which allows more material to desorb at lower temperatures.

3.5.2 ~8 Monolayer Graphene Oxide Crystal

The TPD spectra at a heating rate of $\sim 50 \frac{^{\circ}\text{C}}{\text{min}}$ for an $\sim 8\text{ML}$ sample is shown in Figure 18. The desorption peak maxima for this sample occur at 111°C . In addition, broad maxima at 140°C and 240°C are also observed. The masses with the highest peaks were 18, 44, and 28, corresponding to the water, carbon dioxide, and carbon monoxide molecules.

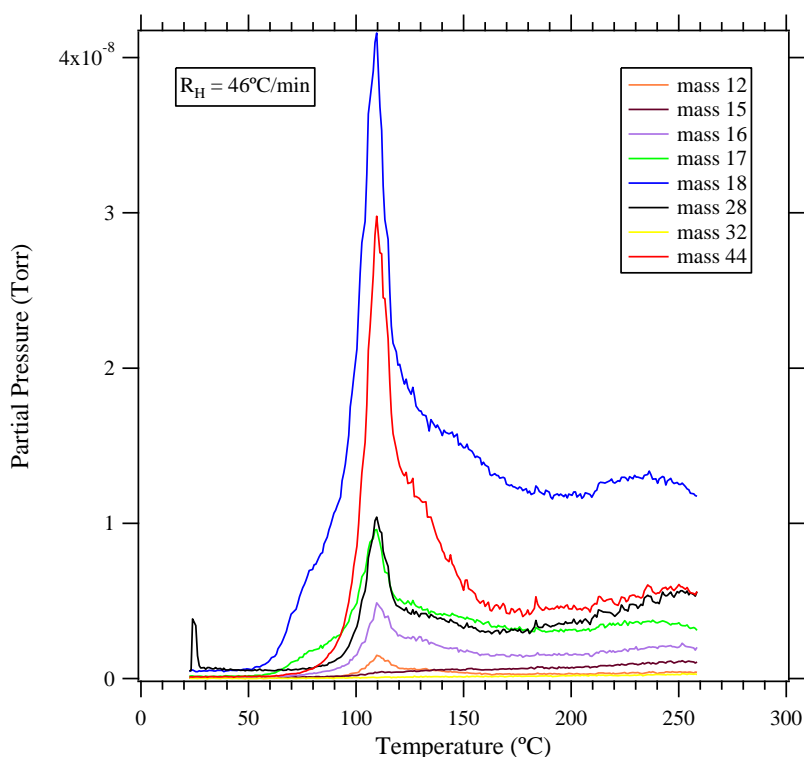


Figure 20: TPD of ~8ML Graphen Oxide.

TPD spectrum of $\sim 8\text{ML}$ graphene oxide heated at a rate of $\sim 50 \frac{^{\circ}\text{C}}{\text{min}}$.

By measuring the areas under the pressure-time curves and correcting for the different RGA sensitivities, the relative amount of carbon dioxide to water and carbon monoxide to water were determined to be 0.25 and 0.19, respectively. The areas under the pressure-

time curves in the ~8 ML samples are expected to decrease by a factor of 3.1 when compared to the ~25 ML set. The ratios that are measured for H₂O, CO₂, and CO are 2.5, 5.3, and 4.2, respectively. This indicates that the composition of the ~8 ML films is slightly different than that of the ~25 ML films.

The double peaks for masses 16 and 17 that were observed in the ~25ML samples are not observed for the ~8 monolayer samples. The masses of 16 and 17 had partial pressure peaks that were consistent with the cracking fractions associated with H₂O, CO₂, and CO. Considering that the thinner samples were produced using a different exfoliation technique, this implies that the most likely introduction of ammonia was during exfoliation. If the ammonia of the thicker samples was solely caused by an interaction with the Si₃N₄ substrate, the thinner samples should also show the lower temperature peak associated with ammonia, but they do not.

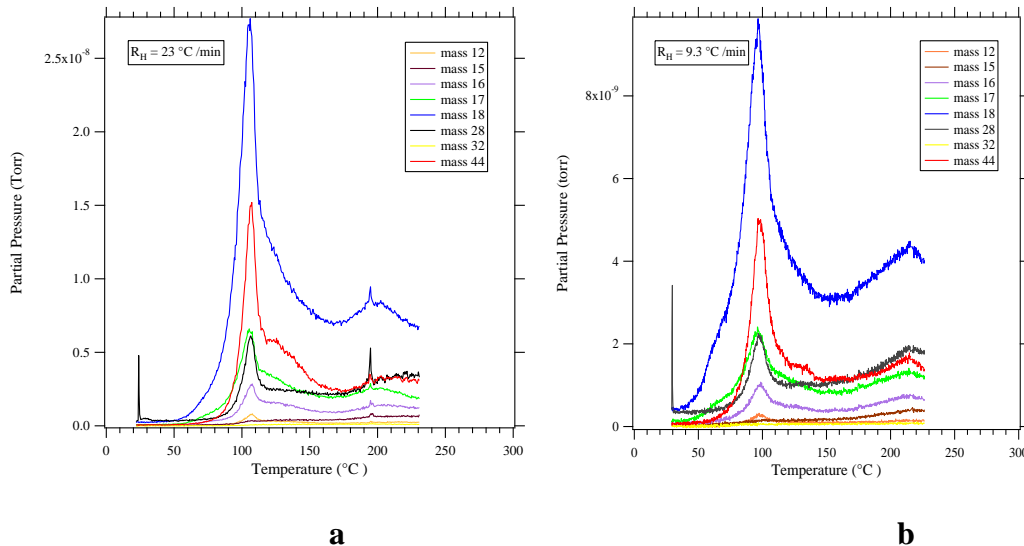


Figure 21: TPD of ~8ML Graphene Oxide at Slower Heating Rates.

TPD spectrum of ~8ML graphene oxide heated at a rate of $\sim 25 \frac{^{\circ}\text{C}}{\text{min}}$ (a) and $\sim 10 \frac{^{\circ}\text{C}}{\text{min}}$ (b). Notice the shift in the desorption peaks to a lower temperature.

3.5.3 ~1 Monolayer Graphene Oxide Crystal

The TPD spectra at a heating rate of $\sim 50 \frac{^{\circ}\text{C}}{\text{min}}$ for an ~1ML sample is shown in Figure 22. The desorption peak maxima for this sample occur at 102°C . At this coverage, the desorption peaks from the graphene oxide are relatively small compared to the signals from the sample holder, which show a slow increase in partial pressure over the whole temperature range of the measurements.

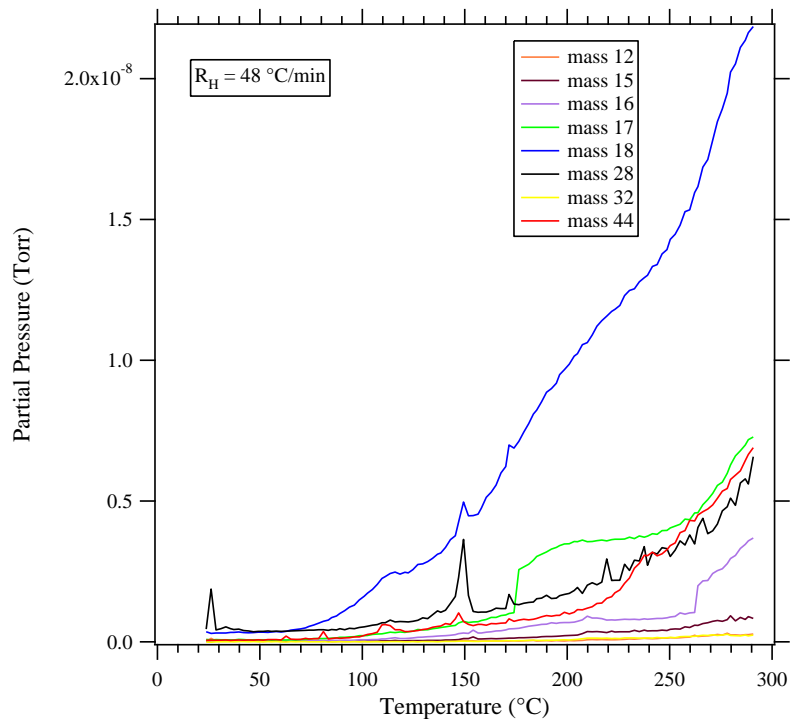


Figure 22: TPD of ~1ML Graphene Oxide.

TPD spectrum of ~1ML graphene oxide heated at a rate of $\sim 50 \frac{^\circ\text{C}}{\text{min}}$.

3.6 Desorption Kinetics

The desorption kinetics of graphene oxide can be identified by comparing the pressure versus temperature spectra of the different sample thicknesses at the same heating rate. As seen in Figure 23 the desorption peaks shift to lower temperatures as the thickness of the sample increases, which follows second order kinetics.

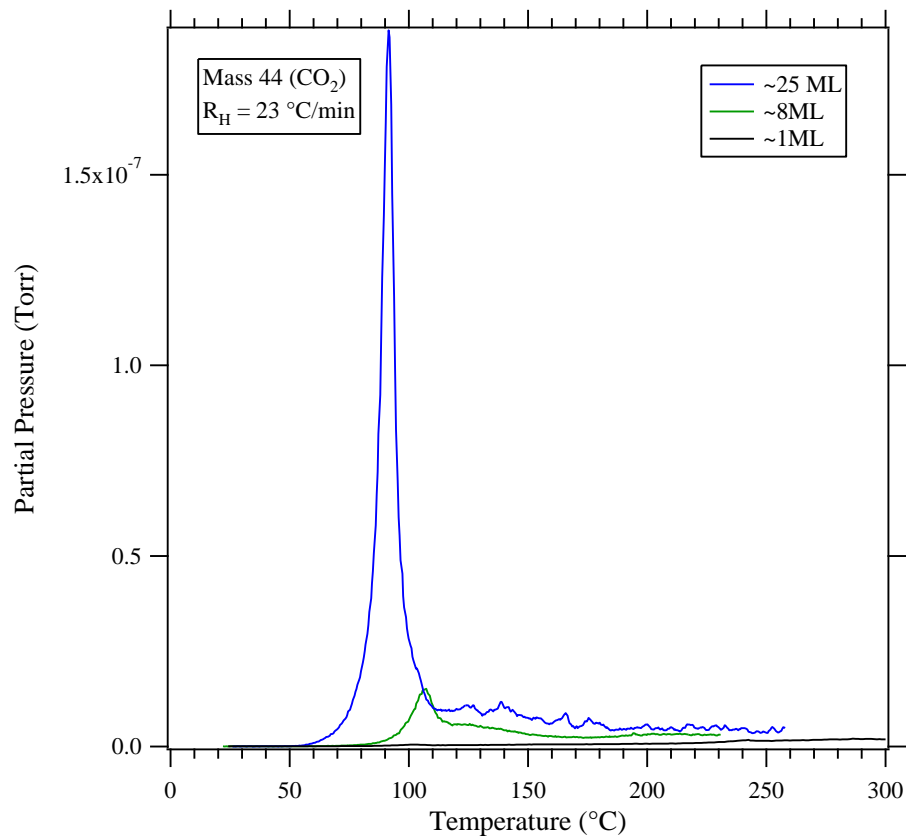


Figure 23: TPD Peaks of CO_2 .

TPD desorption peaks of CO_2 for ~25, ~8, and ~1ML graphene oxide heated at a rate of $\sim 25 \frac{^\circ C}{min}$.

Analyzing the TPD spectrum and the theoretical models of the structure of graphene oxide referenced in the introduction, second order kinetics, which corresponds to recombinational desorption, can be justified. The different theoretical models of graphene oxide show that oxygen only exists as hydroxyl groups or single oxygen atoms bonded to the graphene surface in the form of an epoxide group (C-O-C) or monoxide group (C=O). As seen in the TPD spectra, very little molecular oxygen is being desorbed from the graphene oxide. Therefore, in order to desorb as CO_2 , the single oxygen atoms

must migrate on the surface to find another oxygen atom before desorbing. A similar process is involved for the desorption of H₂O since an additional hydrogen atom is needed before desorption can proceed. Since the CO desorption occurs at the same temperature as the CO₂ and H₂O, the direct desorption of CO must be coupled to the decomposition of the oxide. As the thickness of the graphene oxide is decreased, the TPD measurements of the areas under the temperature-time curves for CO₂ and CO indicate that the thinner films have a lower oxygen concentration. Therefore, the average time that each oxygen atom or hydroxyl group must diffuse across the surface before finding another oxygen atom or hydroxyl group is longer. As time increases, the temperature also increases, giving a temperature shift to higher temperatures for the desorption peaks.

3.7 Activation Energies.

With the kinetics being identified as second order, the activation energies can be calculated via the Redhead method [30]. Since the temperature of the desorption maxima shifts as the graphene oxide coverage increases, it is important to make the TPD measurements with samples that all have the same coverage. Therefore, the activation energy has been found for the ~8ML and ~25ML samples, specifically. By assuming that each sample has the same film thickness within their respective group, it can be assumed that the coverage is the same for each sample. This assumption allows the coverage term within Equation 24 to be ignored when plotting the data. The actual heating rates and temperatures of the desorption maxima for CO₂ are given in Table 2 and Table 3.

Table 2: CO₂ From a ~25ML film

| Desorption Temperature T_p (K) | Heating Rate $\left(\frac{K}{sec}\right)$ |
|-------------------------------------|---|
| 351 | 0.1516 |
| 365 | 0.3852 |
| 376 | 0.7720 |

Actual heating rates and desorption maxima for CO₂ in a ~25ML graphene oxide film.

Table 3: CO₂ From a ~8ML film

| Desorption Temperature T_p (K) | Heating Rate $\left(\frac{K}{sec}\right)$ |
|-------------------------------------|---|
| 372 | 0.1552 |
| 380 | 0.3791 |
| 384 | 0.7637 |

Actual heating rates and desorption maxima for CO₂ in a ~8ML graphene oxide film.

By plotting the $\ln\left(\frac{T_p^2}{\beta}\right)$ as a function of $\frac{1}{T_p}$ and fitting the data to a linear least squares curve, the activation energy for desorption can be calculated by multiplying the slope of the linear fit by the gas constant ($R = 1.987\frac{cal}{K \cdot mol}$). Plots for the ~8 ML and ~25 ML films are shown in Figure 24. The activation energy, T_p , of the ~8ML graphene oxide sample was measured to be 1.48eV.

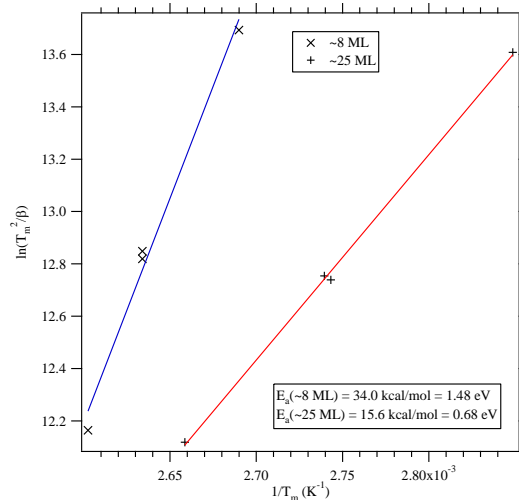


Figure 24: Activation Energies of Graphene Oxide.

Plots finding the activation energies of ~25 and ~8ML graphene oxide using Redhead method.

The activation energy for the ~25ML film was measured to be 0.68eV. The activation energy of the ~25ML is less than half that of the ~8ML film. This difference between the two activation energies qualitatively agrees with the composition data obtained by integrating the TPD peaks, in that the ~8ML film has a different composition than the ~25ML film.

CHAPTER 4

DISCUSSION

Since graphene oxide has potential for use as a nanoscale thick dielectric, understanding its thermal stability is important since the manufacture of devices based on this material may involve processing at elevated temperatures. The TPD measurements show that the oxide begins decomposition at temperatures as low as $\sim 60^\circ\text{C}$ and is almost entirely decomposed by $\sim 150^\circ\text{C}$. Therefore, graphene oxide is a very fragile oxide which would require only low temperature processing techniques for device manufacture.

One of the primary reasons for studying the thermal decomposition of graphene oxide is to determine the feasibility of using graphene oxide as a convenient carbon source for the formation of single-layer graphene. The XPS data show decreases in the carbon peaks, indicating that carbon is possibly desorbing. The TPD data confirms the loss of carbon since there are significant CO_2 and CO peaks during the decomposition of the oxide. The TPD measurements also show that virtually no O_2 desorbs from the sample. Therefore, the crystal structure of graphene oxide is being compromised during the heat treatment.

The XPS spectra show that there is some carbon remaining on the sample surface after the heat treatments. The diffuse patterns observed by LEED after the heat treatment indicates that the carbon remaining on the sample surface is a disordered carbon film. Unlike graphene, disordered carbon is not inert at atmospheric pressures. Therefore, the

O-1s XPS peaks that are observed after high temperature anneals may be caused by re-oxidation and/or adsorption of H₂O and OH groups when the sample is removed from UHV and transported to the University of Texas.

Our data show promise for the reduction graphene oxide into graphene when annealed at very high temperatures. Under UHV conditions, the disordered carbon film will not desorb since there is no source of oxygen. Therefore, this film will remain on the sample surface and should convert to ordered graphene at sufficiently high temperatures. Comparing the XPS spectra of the samples annealed at high temperatures shows a strong correlation between the amount of oxygen on the sample surface and the annealing temperature. Considering that the TPD measurements of graphene oxide indicate that it has mostly decomposed by ~150°C the reduction of oxygen detected by XPS at high temperatures may give evidence for the graphitization of the carbon films. For instance, the sample annealed to 900°C shows a complete disappearance in the XPS peaks associated with the O=C-H and O=C groups, even though it was exposed to atmospheric conditions. The only explanation for this is that the disordered carbon is starting to crystallize into graphene or thin layers of graphite. The oxygen peak that remains after this anneal could be from an oxide layer forming on bare regions of Si₃N₄ or from some of the carbon on the surface that has not recrystallized into graphene. Further high temperature annealing studies of graphene oxide in UHV are needed to confirm this recrystallization effect.

The morphology of graphene oxide as it is annealed could have significant effects when using graphene oxide in devices. There is an obvious change in the morphology of

the film as the temperature increases. The AFM images show that the annealed graphene oxide loses the platelet properties and starts to clump into pyramidal peaks at temperatures as low as 500°C. However, considering the decomposition of the oxide occurs at such a low temperature, the platelet properties are probably gone at a much lower temperature. Even more interesting is the change in the morphology to several rounded structures when the temperature is increased to 700°C. It is uncertain why there is such a drastic change between these two temperatures, but it shows that the increase in temperature is having a direct effect on the disordered carbon. The drastic changes in the morphology into different types of peaks could explain why the Si₃N₄ is partially exposed.

CHAPTER5

CONCLUSION

The overall design and construction of the TPD system, which includes a load lock for sample transfer, has resulted in a measurement system that has provided reproducible TPD results over the temperature range necessary for the decomposition of graphene oxide. The load lock proved to be crucial because of the relatively low decomposition temperature of graphene oxide. By placing the thermocouple on the front of the graphene oxide crystal, accurate readings for the temperature of the graphene oxide during the TPS measurements are obtained. With these two improvements, accurate temperature measurements of the full TPD spectrum of graphene oxide were obtained. By controlling the mass spectrometer and the temperature ramp by computer, the temperature could be increased linearly and multiple masses could be measured simultaneously during the TPD measurements. This has allowed us to perform one of the first studies of the kinetics and the activation energies for the reduction of graphene oxide.

It is apparent from the TPD measurements that if graphene oxide is to be used as a dielectric in devices, only low temperature processing steps can be used for device manufacture. The onset of decomposition of the film at $\sim 60^\circ$ and the rapid changes in the morphology would ultimately make a traditional Si-based device impractical because of the high temperatures needed for oxidation, diffusion of dopants, etc.

The TPD spectra of the ~8ML and ~25ML samples show different activation energies. In addition, the areas under the pressure-time curves for H₂O, CO₂, and CO do not all scale with the nominal graphene oxide thickness. Therefore, there seems to be an inconsistency in the extent of oxidation of the graphene oxide that is dependent on the sample thickness. Future research will need to address why this is occurring before graphene oxide will be a viable material for devices.

The results do show promise for the reduction of graphene oxide into graphene under UHV conditions. The reduction of the O=C-OH, C-OH, C-O-C, and O=C peaks measured by XPS and the change in morphology as temperature is increased above 500 °C gives a positive outlook for the reduction of graphene oxide to graphene within UHV. Therefore, obtaining TPD spectra at temperatures above ~400 °C, which is the current temperature limit of our system, is essential for the future of this research. Minor changes to the TPD system will be required to reach the desired temperatures. The preamp was not design for the high voltages that are required for electron beam heating. This will require the redesign of the preamp so that an isolation amplifier can be used to isolate the instrumentation amplifier of the preamp from the high voltage offset of the thermocouple. The XPS data provide evidence that at 900°C graphitization of the reduced graphene oxide has begun. However, the temperature to fully graphitize the disordered carbon remaining after decomposition will most likely be higher. Therefore, it is essential to integrate electron beam heating into the current TPD system.

APPENDIX

Cracking Patterns

From Hiden Analytical

<http://www.hidenanalytical.com/>

Wednesday, 25 June 2008 17:11

| | | peak 1 | | peak 2 | | peak 3 | | rel | |
|-----------|----------------------|--------|-------|--------|-------|--------|-------|------|------|
| | | | m/z % | | m/z % | | m/z % | sens | |
| 1 | acetone | C3H6O | 43 | 100 | 58 | 33 | 15 | 20 | 3.6 |
| 2 | air | | 28 | 100 | 32 | 27 | 14 | 6 | 1.0 |
| 3 | ammonia | NH3 | 17 | 100 | 16 | 80 | 15 | 8 | 1.3 |
| 4 | argon | Ar | 40 | 100 | 20 | 16 | 36 | 0.3 | 1.2 |
| 5 | benzene | C6H6 | 78 | 100 | 77 | 19 | 52 | 16 | 5.9 |
| 6 | boron trichloride | BCl3 | 81 | 100 | 83 | 65 | 35 | 29 | 1.0 |
| 7 | carbon dioxide | CO2 | 44 | 100 | 16 | 9 | 28 | 8 | 1.4 |
| 8 | carbon monoxide | CO | 28 | 100 | 12 | 5 | 16 | 2 | 1.05 |
| 9 | carbon tetrafluoride | CF4 | 69 | 100 | 50 | 12 | 19 | 7 | 1.0 |
| 10 | diborane | B2H6 | 26 | 100 | 27 | 97 | 24 | 90 | 1.0 |
| 11 | ethane | C2H6 | 28 | 100 | 27 | 33 | 30 | 26 | 2.6 |
| 12 | ethanol | C2H5OH | 31 | 100 | 45 | 51 | 29 | 30 | 3.6 |
| 13 | Fomblin oil | | 69 | 100 | 20 | 28 | 16 | 16 | 1.0 |
| 14 | Freon 12 | CCl2F2 | 85 | 100 | 87 | 32 | 50 | 16 | 2.7 |
| 15 | helium | He | 4 | 100 | | | | | 0.14 |
| 16 | hydrogen | H2 | 2 | 100 | 1 | 2 | | | 0.44 |
| 17 | hydrogen chloride | HCl | 36 | 100 | 38 | 32 | 35 | 17 | 1.6 |

Cracking Patterns (Continued)

| | | peak 1 | | peak 2 | | peak 3 | | rel | |
|-----------|-----------------------|--------|-------|--------|-------|--------|-------|------|------|
| | | | m/z % | | m/z % | | m/z % | sens | |
| 18 | hydrogen sulphide | H2S | 34 | 100 | 32 | 44 | 33 | 42 | 2.2 |
| 19 | isopropyl alcohol | C3H7OH | 45 | 100 | 43 | 14 | 27 | 9 | 1.0 |
| 20 | krypton | Kr | 84 | 100 | 86 | 31 | 82 | 21 | 1.7 |
| 21 | methane | CH4 | 16 | 100 | 15 | 85 | 14 | 16 | 1.6 |
| 22 | methanol | CH3OH | 31 | 100 | 32 | 67 | 29 | 65 | 1.8 |
| 23 | neon | Ne | 20 | 100 | 22 | 10 | 21 | 0.3 | 0.23 |
| 24 | nitrogen | N2 | 28 | 100 | 14 | 5 | 29 | 1 | 1.0 |
| 25 | oxygen | O2 | 32 | 100 | 16 | 9 | | | 0.86 |
| 26 | phosphine | PH3 | 34 | 100 | 33 | 33 | 31 | 32 | 2.6 |
| 27 | pump oil | | 57 | 100 | 55 | 73 | 43 | 73 | 1.0 |
| 28 | silane | SiH4 | 30 | 100 | 31 | 78 | 29 | 29 | 1.0 |
| 29 | silicon tetrafluoride | SiF4 | 85 | 100 | 86 | 5 | 28 | 4 | 1.0 |
| 30 | sulphur dioxide | SO2 | 64 | 100 | 48 | 50 | 32 | 10 | 2.1 |
| 31 | water | H2O | 18 | 100 | 17 | 21 | 16 | 2 | 0.9 |
| 32 | xenon | Xe | 132 | 100 | 129 | 98 | 131 | 79 | 3.0 |

REFERENCES

1. Geim, A. K. and Novoselov, K. S., *The rise of graphene*. Nat. Mater., 2007. 6: p. 183-191.
2. Berger, C. et al. *Ultrathin epitaxial graphite: 2D electron gas properties and a route toward graphene-based nanoelectronics*. J. Phys. Chem. B, 2004. 108: p. 19912-19916.
3. Novoselov, K. S. et al. *Electric field effect in atomically thin carbon films*. Science 306, 666–669 (2004).
4. Novoselov, K. S. et al. *Two-dimensional atomic crystals*. Proc. Natl Acad. Sci. USA 102, 10451–10453 (2005).
5. Novoselov, K. S. et al. *Two-dimensional gas of massless Dirac fermions in graphene*. Nature 438, 197–200 (2005).
6. Ohta, T., Bostwick, A., Seyller, T., Horn, K. & Rotenberg, E. *Controlling the electronic structure of bilayer graphene*. Science 313, 951–954 (2006).
7. Zhang, Y., Tan, J. W., Stormer, H. L. & Kim, P. *Experimental observation of the quantum Hall effect and Berry's phase in graphene*. Nature 438, 201–204 (2005).
8. Krishnan, A. et al. *Graphitic cones and the nucleation of curved carbon surfaces*. Nature 388, 451–454 (1997).
9. Land, T. A., Michely, T., Behm, R. J., Hemminger, J. C. & Comsa, G. *STM investigation of single layer graphite structures produced on Pt(111) by hydrocarbon decomposition*. Surf. Sci. 264, 261–270 (1992).
10. Nagashima, A. et al. *Electronic states of monolayer graphite formed on TiC(111) surface*. Surf. Sci. 291, 93–98 (1993).
11. Berger, C. et al. *Electronic confinement and coherence in patterned epitaxial graphene*. Science 312, 1191–1196 (2006).
12. Ohta, T., Bostwick, A., Seyller, T., Horn, K. & Rotenberg, E. *Controlling the electronic structure of bilayer graphene*. Science 313, 951–954 (2006).

13. Dikin D. A., Stankovich S., Zimney E. J., Piner R. D., Dommett G. H. B., Evmenenko G., *et. al.* *Preparation and Characterization of graphene oxide paper.* Nature 2007;448(7152):457-60.
14. Li D., Müller M. B., Gilje S., Kaner R. B., & Wallace G. G., *Processable aqueous dispersions of graphene nanosheets.* Nature Nanotechnol 2008;3(2): 101-15.
15. Szabo, T., Berkesi, O., Forgo, P., Josepovitis, K., Sanakis, Y., Petridis, D., & Dekany, I., *Evolution of surface functional groups in a series of progressively oxidized graphite oxides.* Chem. Mater., 2006. 18: p. 2740-2749.
16. Chen, H., Müller, M. B., Gilmore, K. J., Wallace, G. G., & Li, D., *Mechanically strong, electrically conductive, and biocompatible graphene paper.* Adv. Mater., 2008. 18: p. 3557-3561.
17. Gilje, S., Han, S., Wang, M., Wang, K. L., & Kaner, R. B., *A chemical route to graphene for device applications.* Nano Letters, 2007. 7(11): p. 3394-3398.
18. Kudin, K. N., Ozbas, B., Schniepp, H. C., Prud'homme, R. K., Aksay, I. A., & Car, R., *Raman spectra of graphite oxide and functionalized graphene sheets.* Nano Letters, 2008. 8(1): p. 36-41.
19. Si, Y. & Samulski, E. T., *Synthesis of water soluble graphene.* Nano Letters, 2008. 8(6): p. 1679-1682.
20. Stankovich, S., Dikin, D. A., Dommett, G. H. B., Kohlhaas, K. M., Zimney, E. J., Stach, E. A., Piner, R. D., Nguyen, S. T., & Ruoff, R. S., *Graphene-based composite materials.* Nature, 2006. 442: p. 282-286.
21. Stankovich, S., Dikin, D. A., Piner, R. D., Kohlhaas, K. M., Kleinhammes, A., Jia, Y., Wu, Y., Nguyen, S. T., & Ruoff, R. S., *Synthesis of graphene-based nanosheets via chemical reduction of exfoliated graphite oxide.* Carbon, 2007. 45: p. 1558-1565.
22. Jung, I., Dikin, D. A., Piner, R. D., & Ruoff, R. S., *Tunable electrical conductivity of individual graphene oxide sheets reduced at "low" temperature.* Nano Letters, 2008. **in press.**
23. UK Surface Analysis Forum. *Surface Science Techniques: Introduction to UHV - Ultra High Vacuum.* <http://www.uksaf.org/tch/uhv.html> (accessed September 17, 2008).
24. Hubbard, Arthur. *The Handbook of Surface Imaging and Visualization.* Boca Raton: CRC Press, 1995.

25. Pendry, J. B. *Low Energy Electron Diffraction*. London: Academic Press, 1974.
26. Kuipers, Ertl. *Low Energy Electrons and Surface Science Chemistry*. Weinheim: Verlag Chemie, 1974.
27. DiNardo, N. John. *Nanoscale Characterization of Surfaces and Interfaces*. Weinheim, Germany: VCH Verlagsgesellschaft, 1994.
28. Moulder, Stickle, Sobol, & Bomben. *Handbook of X-ray Photoelectron Spectroscopy: A Handbook of Standard Spectra for Identification and Interpretation of XPS Data*. Eden Prairie: Physical Electronics, 1995.
29. Hubbard, Arthur. *The Handbook of Surface Imaging and Visualization*. Boca Raton: CRC Press, 1995.
30. Chiu, C. M., & D. C. Muddiman. *American Society for Mass Spectrometry*. <http://www.asms.org/whatisms/> (accessed November 4, 2008).
31. Redhead, P. A. *Thermal Desorption of Gases*. *Vacuum* vol 12, 1962: 203-211.
32. D. Yang, A. Velamakanni, G. Bozoklu, A. Park, M. Stoller, R. D. Piner, S. Stankovich, I. Jung, D. A. Field, C. A. Ventrice, & R. S. Ruoff. *Chemical Analysis of Graphene Oxide Films After Heat and Chemical Treatments by X-ray Photoelectron and Micro-Raman Spectroscopy*. *Carbon*, 2008: **in press**.
33. *Omega Complete Temperature Measurement Handbook and Encyclopedia: Type K Thermocouple Temperature Coefficients*. Vol 28, Omega Engineering, 1992.

VITA



Daniel Alexander Field is the youngest son of Quinten and Hannelore Field. He was born in Waco, Texas on December 20, 1983, and was raised outside of Waco in the rural town of Speegleville.

Daniel attended the schools of Midway Independent School District before graduating in May 2002. In August 2002, Daniel enrolled at Sam Houston State University. At Sam Houston he performed undergraduate research in astronomy until he was awarded a Bachelor of Science in December 2006.

The following January, Daniel enrolled at Texas State University-San Marcos to pursue his master's in applied physics. He began his graduate research in January 2008, emphasizing on temperature programmed desorption of graphene oxide. He expects to graduate as Master of Physics in May 2009.

Daniel plans to continue his education and obtain a Ph.D. in physics. He would like to stay in academia, instructing and doing research. However, for now he will sit back, take it easy, and look forward to the future, the future that is physics.

Permanent Address: 172 Wandering Oaks Rd.

Waco, Texas 76712

This thesis was typed by Daniel Alexander Field.